This is a preprint, the final version is subject to change, of the American Mineralogist (MSA)
Cite as Authors (Year) Title. American Mineralogist, in press.
(DOI will not work until issue is live.) DOI: http://dx.doi.org/10.2138/am-2017-6162

REVISION 1

The equation of state of wadsleyite solid solutions: Constraining the effects of anisotropy and crystal chemistry

Johannes Buchen[1]* (johannes.buchen@uni-bayreuth.de),
Hauke Marquardt[1] (hauke.marquardt@uni-bayreuth.de),
Tiziana Boffa Ballaran[1] (tiziana.boffa-ballaran@uni-bayreuth.de),
Takaaki Kawazoe[1] (takaaki.kawazoe@uni-bayreuth.de),
Catherine McCammon[1] (catherine.mccammon@uni-bayreuth.de)
[1] Bayerisches Geoinstitut, Universität Bayreuth, 95440 Bayreuth, Germany
* Corresponding author

Abstract

A quantitative knowledge of the equation of state of wadsleyite solid solutions is needed to refine thermodynamic and thermoelastic models for the transition zone in Earth's upper mantle. Here we present the results of high-pressure single-crystal X-ray diffraction experiments on two crystals of slightly hydrous iron-bearing wadsleyite with Fe/(Mg+Fe) = 0.112(2), $Fe^{3+}/\sum Fe$ = 0.15(3), and 0.24(2) wt% H_2O up to 20 GPa. By compressing two wadsleyite crystal sections inside the same diamond anvil cell, we find a negligible influence of crystal orientation on the derived equation of state parameters. Volume and linear compression curves were analyzed with finite strain theory to demonstrate their mutual consistency for the Reuss bound indicating quasi-hydrostatic stress conditions. The results on the here-studied wadsleyite crystals are incorporated into a multi-end member model to describe the equation of state for wadsleyite solid solutions in the system Mg_2SiO_4-Fe_2SiO_4-MgH_2SiO_4-Fe_3O_4. For the hypothetical ferrous

wadsleyite end member, Fe_2SiO_4, we find a substantially larger bulk modulus than expected by extrapolating currently accepted trends. The multi-end member equation of state model may serve as a basis for the calculation of phase equilibria and the interpretation of seismic observations regarding the transition zone.

Keywords

Wadsleyite, transition zone, equation of state, solid solution, diamond anvil cell

Introduction

In most models for Earth's upper mantle, wadsleyite, β-$(Mg,Fe)_2SiO_4$, is assumed to be a major phase in the transition zone (Ringwood 1991; Frost 2008; Stixrude and Lithgow-Bertelloni 2011). The steep increase in seismic velocities around 410 km depth has been attributed to the phase transition of olivine, α-$(Mg,Fe)_2SiO_4$, to wadsleyite (Bina and Wood 1987; Ringwood 1991; Agee 1998). Seismological observables related to the 410-km discontinuity such as the magnitude, depth, and depth interval of the velocity and density increase (Shearer 2000; Houser 2016) serve as anchor points to constrain the mineralogical, chemical, and thermal state of the upper mantle (Katsura et al. 2010; Wang et al. 2014; Chang et al. 2015; Zhang and Bass 2016).

In addition to iron-magnesium substitution (Ringwood and Major 1970; Frost 2003), nominally anhydrous wadsleyite can incorporate substantial amounts of hydrogen (Smyth 1994; Inoue et al. 1995) in the form of hydroxyl groups (McMillan et al. 1991; Young et al. 1993). Moreover, wadsleyites with $Fe^{3+}/\sum Fe$ up to 96 % have been synthesized under oxidizing conditions (Smyth et al. 1997; McCammon et al. 2004). Both hydrogen and ferric iron expand the stability field of wadsleyite to lower pressures and affect the pressure interval of the phase transition (Wood 1995; Smyth and Frost 2002; Frost and Dolejš 2007; Frost and McCammon

2009). To describe phase equilibria and to model seismic properties of wadsleyite, we need to know the equation of state (EOS) for wadsleyite solid solutions spanning the range of relevant compositions as captured by the system Mg_2SiO_4-Fe_2SiO_4-MgH_2SiO_4-Fe_3O_4.

The variation of individual EOS parameters as a function of wadsleyite crystal chemistry has been addressed in previous studies, and certain trends have been established. Both iron and hydrogen incorporation expand the unit cell at ambient conditions but have opposing effects on the density (Finger et al. 1993; Holl et al. 2008; Mao et al. 2008b). While the incorporation of hydrogen clearly enhances the compressibility of wadsleyite (Holl et al. 2008; Mao et al. 2008b; Ye et al. 2010; Chang et al. 2015), the bulk modulus appears to be insensitive to iron-magnesium exchange when directly comparing experimental values determined with different techniques and based on different EOS assumptions (Wang et al. 2014; Chang et al. 2015). Only few studies addressed the combined effect of iron and hydrogen on the EOS of wadsleyite indicating that iron slightly counteracts the reduction of the bulk modulus due to hydrogen incorporation (Mao et al. 2011; Chang et al. 2015; Mao and Li 2016).

Although ferric iron was shown to stabilize wadsleyite at lower pressures and to broaden the 410-km discontinuity (Frost and McCammon 2009), little is known about the effect of the Fe^{3+} cation on the elastic properties of wadsleyite. Hazen et al. (2000b) deduced a negligible effect of ferric iron on the compression behavior from their high-pressure single-crystal X-ray diffraction study on $Fe_{2.33}Si_{0.67}O_4$, a member of the low-pressure spinelloid III solid solution series (Woodland and Angel 1998, 2000; Koch et al. 2004). This solid solution series is isostructural with wadsleyite and spanned by the coupled substitution of octahedral Mg^{2+} and Fe^{2+} cations and tetrahedral Si^{4+} by ferric iron (Woodland and Angel 1998; Hazen et al. 2000b; Woodland et al. 2012). The fact that in many studies on the EOS of iron-bearing wadsleyites the

amount of ferric iron has not been assessed could mask a potential impact of ferric iron on the elastic properties of wadsleyite solid solutions.

In the case of orthorhombic minerals like wadsleyite, single crystals respond to compression with anisotropic strain. This compressional anisotropy bears the potential to bias extracted equation of state parameters in the presence of deviatoric stresses (Meng et al. 1993; Zhao et al. 2010). By comparing the compression behavior for crystals with different orientations relative to the stress field, potential bias due to deviatoric stresses should become apparent. Moreover, linear and bulk compressibilities derived from quasi-hydrostatic compression experiments should be mutually consistent for the Reuss bound (Angel 2000; Angel et al. 2014).

Here we present the results of high-pressure single-crystal X-ray diffraction experiments on slightly hydrous iron-bearing wadsleyite with Fe/(Mg+Fe) = 0.112(2), $Fe^{3+}/\sum Fe$ = 0.15(3), and 0.24 wt% H_2O up to 20 GPa. Two crystals of the same composition were loaded together into the same pressure chamber of a diamond anvil cell (DAC) but with different crystallographic orientations relative to the compression axis. This setup aimed to detect any influence of crystal orientation on the derived EOS that may result from deviatoric stresses inside the DAC at high pressures. We analyzed volume and axial compression curves of both crystals with finite strain equations of state to find mutually consistent descriptions of bulk and anisotropic compression. To describe anisotropic compression, we derived a linear EOS for each crystallographic axis.

We further reanalyzed available compression data employing a consistent analysis scheme and constructed a model for the EOS of wadsleyite solid solutions in the system Mg_2SiO_4-Fe_2SiO_4-MgH_2SiO_4-Fe_3O_4. The model captures the variation of unit cell volume and bulk modulus as a function of iron and hydrogen content. We extended this model to describe the anisotropic compression behavior of wadsleyite solid solutions by including single-crystal elasticity and anisotropic compression data.

96

97 ## Experimental

98 ### Single-crystal synthesis and chemical composition

99 Wadsleyite single crystals with sizes up to 500 μm were synthesized from San Carlos
100 olivine powder in a 1000-ton multi-anvil press (run H4015). Details of the crystal synthesis have
101 been reported elsewhere (Kawazoe et al. 2015). Four grains were mounted in resin and polished
102 for subsequent electron microprobe analysis (EMPA) (15 kV, 15 nA, 1-2 μm beam diameter).
103 Line scans indicated chemical homogeneity both for single grains and among different grains
104 with Fe/(Mg+Fe) = 0.112(2) and M/Si = 1.92(1) where M stands for all analyzed metals (Mg, Fe,
105 Ni, Ca, Al, Mn) other than silicon. Complete results of the EMPA are summarized in Table S1[1].

106

107 ### Mössbauer spectroscopy

108 A mixture of fine-grained material and several coarser grains was ground to a
109 homogeneous powder and loaded into a hole in a 1 mm thick lead sheet with a diameter of 500
110 μm. Based on the physical thickness and chemical composition, we estimate the Mössbauer
111 thickness to be 15 mg Fe/cm^2. The lead sheet containing the powder was subsequently mounted
112 in front of the ^{57}Co point source (nominal activity 370 MBq over 500 x 500 μm^2) of a constant
113 acceleration Mössbauer spectrometer. A Mössbauer spectrum was recorded at room temperature
114 in transmission mode for 2 days. The velocity scale was calibrated using certified line positions
115 of α-Fe (former National Bureau of Standards material no. 1541) and a Mössbauer spectrum
116 collected on a 25 μm thick α-Fe foil.

117 The spectrum recorded on the wadsleyite powder was analyzed by fitting a series of
118 Lorentzian functions to the transmission minima using the program MossA (Prescher et al. 2012).
119 We applied five different fitting models based on Mössbauer spectral analyses of wadsleyite

120 reported by Mrosko et al. (2015) and Kawazoe et al. (2016) to explore the sensitivity of the
121 parameters to the model used. Details about the individual models can be found in the
122 supplemental online material[1]. The amount of Fe^{3+} as represented by the relative area of its
123 absorption is independent of the applied fitting model within the experimental uncertainty. Our
124 preferred fit is shown in Figure S1[1] with the parameters listed in Table S2[1] and yields $Fe^{3+}/\sum Fe$ =
125 0.15(3).
126
127 **Single-crystal X-ray diffraction at ambient conditions**
128 Single crystals of at least 300 μm in size that showed uniform extinction when viewed
129 between crossed polarizers were selected and glued onto a glass fiber for single-crystal X-ray
130 diffraction. Crystal quality was assessed by scanning reflections on a Huber 4-circle Eulerian
131 cradle diffractometer operating with Mo-*K*α radiation generated at 40 kV and 20-30 mA and a
132 point detector. A total of 26 reflections were collected for two wadsleyite crystals with full
133 widths at half peak heights of ω scans between 0.06° and 0.15° using the 8-position centering
134 protocol (King and Finger 1979) implemented in the SINGLE program (Angel and Finger 2011).
135 Unit cell parameters were refined assuming orthorhombic and monoclinic symmetry with space
136 groups *Imma* (Horiuchi and Sawamoto 1981) and *I*2/*m* (Smyth et al. 1997), respectively. Since
137 unit cell edge lengths and volumes were identical within errors for both symmetries, only the
138 orthorhombic values are summarized in Table 1 together with further X-ray diffraction results.
139 The crystals, however, showed monoclinic distortions, $\beta > 90°$, (Table 1) that fall in the range
140 observed for wadsleyites of different hydration states (Smyth et al. 1997; Kudoh and Inoue 1999;
141 Jacobsen et al. 2005; Holl et al. 2008; Mao et al. 2008b). After being oriented on the
142 diffractometer as described by Jacobsen et al. (2005), the crystals were double-sided polished to

plane-parallel thin sections parallel to either the (120) or (243) crystallographic planes, hereafter referred to as X120 and X243, respectively, with a final thickness of 10(1) μm.

Fourier transform infrared absorption spectroscopy

Polarized and unpolarized infrared absorption spectra were recorded on X120 and X243 with a Bruker IFS 120 HR Fourier transform infrared (FTIR) spectrometer in a spectral range from 2500 cm^{-1} to 4000 cm^{-1} (see supplemental online material[1] for details). By comparing spectra collected on at least 5 different spots on each crystal with spot diameters between 100 μm and 200 μm, we found the infrared absorption to be homogeneous across each crystal section. For polarized spectra, the electric field vector **E** was oriented parallel to each of the two vibration directions, *n'* and *n"*, as determined from the extinction positions of the single-crystal thin sections between crossed polarizers in visible light. Representative infrared absorption spectra for both crystal orientations, (120) and (243), are shown in Figures S2a and S2b[1].

All spectra were dominated by two absorption bands centered around 3340 cm^{-1} and 3600 cm^{-1} (Figures S2 and S3[1]). These bands correspond to the most prominent absorption features attributed to structurally bonded hydroxyl groups in wadsleyite (e.g. McMillan et al. 1991; Young et al. 1993; Jacobsen et al. 2005). To calculate total absorbances A_{TOT} and hydrogen contents from the polarized spectra, we made use of the principles explained by Libowitzky and Rossman (1996) and the crystal symmetry of wadsleyite (crystal class *mmm*) (Figure S4[1]). To facilitate comparison between different calibrations and hydrogen contents reported in earlier work, we evaluated hydrogen concentrations with calibrations by Libowitzky and Rossman (1997), Paterson (1982), and Deon et al. (2010). Band specific absorbances, mean wavenumbers, and hydrogen concentrations are summarized in Table S3[1]. More details can be found in the supplemental online material[1]. Although we obtained identical total hydrogen concentrations

when applying the calibrations by Deon et al. (2010) and Libowitzky and Rossman (1997), we emphasize that band specific hydrogen concentrations differ significantly between these calibrations (Table S3[1]). These differences demonstrate that the redistribution of absorption strength among bands at different frequencies as previously observed for iron-bearing wadsleyites (Bolfan-Casanova et al. 2012; Smyth et al. 2014) requires a wavenumber-dependent molar absorption coefficient as included in the calibrations by Libowitzky and Rossman (1997) and Paterson (1982). According to the calibration of Libowitzky and Rossman (1997), we found total hydrogen contents of 0.26(2) wt% H_2O for X120 and 0.22(2) wt% H_2O for X243. In view of the analytical uncertainties, both hydrogen contents are identical, and we use their mean value 0.24(2) wt% H_2O for both crystals.

Sample preparation and high-pressure experiments

After characterization by FTIR spectroscopy, the thin sections were glued onto metallic carriers and inserted into a FEI Scios dual beam device. A Ga^+ ion beam operated at an acceleration voltage of 30 kV was used to cut circular disks with diameters of 110 μm out of the single-crystal thin sections (Marquardt and Marquardt 2012). In a second step, the circles were cut in half to semicircles. The ion beam current was adjusted between 7 nA and 30 nA depending on crystal thickness and available machine time (Schulze et al. 2017).

Two semicircles of complementary orientations, i.e. one oriented parallel to (120), X120, and one parallel to (243), X243, were loaded together into a BX90 diamond anvil cell (DAC) (Kantor et al. 2012) equipped with diamond anvils of 500 μm culet size and tungsten carbide seats. The compression axis of the DAC was oriented along the plane normals, i.e. along the reciprocal lattice vectors (120) and (243). The symmetry equivalents of these vectors form pairs of almost perpendicular directions (Figure S4[1]). The pressure chamber was formed by a circular

hole with a diameter of 275 μm cut with an infrared laser in the center of the culet indentation of a rhenium gasket preindented to a thickness of about 60 μm. Neon gas precompressed to about 1.3 kbar was loaded as a pressure transmitting medium using the gas loading system at the Bayerisches Geoinstitut (Kurnosov et al. 2008). Solid neon was shown to create a quasi-hydrostatic stress environment up to 15 GPa (Meng et al. 1993; Klotz et al. 2009). For pressure determination, a ruby sphere was loaded into the DAC together with the crystal segments.

High-pressure single-crystal X-ray diffraction

At high pressures, the lattice constants of the crystals inside the DAC were determined by single-crystal X-ray diffraction on the same diffractometer system as described above, now operated at 50 kV and 40 mA. Before gas loading, the lattice constants were obtained at ambient conditions with the specimens residing inside the DAC. Final ω scans were inspected and refit with the program WinIntegrStp (Angel 2003). Profiles of low quality resulting in unreliable fits were rejected. At each pressure, the lattice constants were refined assuming first an orthorhombic and then a monoclinic unit cell. The number of reflections included in the refinements varied as a result of rejecting poor-quality profiles. For X120, unit cell parameters were computed using 16 to 20 reflections of the families 013, 211, 103, 141, 033, 231, 004, 240, 204, 105, 341, 244, and 271 with $15° < 2\theta < 30°$ and, for X243, using 11 to 20 reflections of the families 013, 211, 103, 141, 033, 231, 240, 053, 204, 105, 303, 341, 244, 073, 271, 413, 305, 084, and 404 with $15° < 2\theta < 36°$.

Results and Discussion

Equation of state

Since both volume and linear incompressibilities for orthorhombic and monoclinic unit cells, including the symmetry-adapted dimensions $a\sin\beta$ and $c\sin\beta$, turned out to be indistinguishable within their uncertainties, we restrict the following discussion to orthorhombic symmetry. This approximation is further justified by the fact that we could not resolve a systematic change of the monoclinic angle β with pressure. For both crystals, orthorhombic unit cell volumes V and edge lengths a, b, and c are compiled in Table 2 and plotted in Figure 1 as a function of pressure P. Differences in the unit cell dimensions between the two crystals amount to less than 0.1 % at the highest pressure (Figure S5[1]) and remain on the same order of magnitude as the experimental uncertainties.

Following previous high-pressure single-crystal X-ray diffraction studies on wadsleyite (Yusa and Inoue 1997; Hazen et al. 2000a, 2000b; Holl et al. 2008; Ye et al. 2010; Chang et al. 2015), the volume compression was described by a third-order Birch-Murnaghan (BM-3) EOS (Birch 1947)

$$P = \left(1 + 2f_{\mathrm{E}}\right)^{5/2}\left(3K_0 f_{\mathrm{E}} + \frac{9}{2}K_0\left(K_0' - 4\right)f_{\mathrm{E}}^2\right) \quad (1)$$

with the isotropic Eulerian finite strain $f_{\mathrm{E}} = [(V_0/V)^{2/3} - 1]/2$, the unit cell volume V_0, the bulk modulus K_0, and its first pressure derivative K_0' at ambient conditions. The variation of normalized pressure F_{E} with Eulerian finite strain f_{E} indicated a third-order contribution of the finite strain (Angel 2000) (Figure S6[1]).

To reveal any difference in compressional behavior between the two crystal sections oriented differently relative to the compression axis of the DAC, each crystal was first treated separately. The resulting unit cell volumes at ambient conditions overlap within their

uncertainties. Furthermore, we found identical bulk moduli and related pressure derivatives for the two crystals (Table 3). These results demonstrate that both crystal sections follow a common compression behavior irrespective of their orientation relative to the compression axis of the DAC. We therefore combined both *P*-*V* datasets in a single EOS and obtained V_0 = 542.09(7) Å^3 and K_0 = 167(1) GPa with K_0' = 4.4(2).

Anisotropic compression behavior and the stress state inside the diamond anvil cell

To describe the anisotropic compression behavior, we followed the approach outlined by Angel (2000) and Angel et al. (2014) who proposed to substitute the volume in an EOS with the cube of a unit cell edge length. This results in the linear BM-3 EOS

$$P = (1 - 2E_i)^{5/2}\left(-k_{i0}E_i + \frac{1}{2}k_{i0}(k'_{i0} - 12)E_i^2\right) \quad (2)$$

with the linear moduli k_{i0}, their pressure derivatives k_{i0}', and the components of the Eulerian finite strain tensor $E_i = [1 - (a_{i0}/a_i)^2]/2$ (i = 1, 2, or 3 for a, b, or c, respectively). Again, each crystal was treated separately first, and the linear moduli for the two crystals overlap within their uncertainties (Table 3). The linear moduli pressure derivatives differ slightly for the two crystals but still overlap within their 2σ uncertainty intervals. In analogy to the volume EOS, we combined both datasets in a single linear EOS for compression along each crystallographic axis. As for volume compression, the anisotropic compression behavior appears to be independent of how the crystal section is oriented relative to the compression axis of the DAC.

Using the two crystal orientations as determined by X-ray diffraction and the derived linear moduli (Table 3), we calculated the effect of potential deviatoric stresses on volume strain using equation 12 of Zhao et al. (2010). Crystal X243 is oriented parallel (243) so that the compression axis of the DAC intersects all three crystallographic axes at nearly equal angles

(Figure S4[1]). In this orientation, the volume strain should be almost insensitive to deviatoric stresses (Zhao et al. 2010). For crystal X120, in contrast, the effect of deviatoric stresses on volume strain is predicted to be an order of magnitude larger than for crystal X243. Since we observed only negligible differences between the unit cell volumes of both crystals (Table 2, Figure S5[1]), we conclude that deviatoric stresses were not large enough to significantly affect the volume strain.

For hydrostatic stress conditions (Reuss bound, Reuss 1929; Watt et al. 1976), the linear moduli can be expressed in terms of single-crystal compliances s_{ij} as $k_i^{\mathrm{R}} = 1/(s_{i1} + s_{i2} + s_{i3})$ (Angel et al. 2014). For isotropic strain conditions (Voigt bound, Voigt 1928; Watt et al. 1976), the linear moduli can be calculated from single-crystal stiffnesses c_{ij} as $k_i^{\mathrm{V}} = c_{i1} + c_{i2} + c_{i3}$. According to these relations, the linear moduli can be combined to the respective bulk moduli (Watt et al. 1976; Nye 1985; Haussühl 2007):

Reuss bound (hydrostatic stress): $$K_0^{\mathrm{R}} = 1/\sum_i \left(s_{i10} + s_{i20} + s_{i30}\right) = 1/\sum_i k_{i0}^{\mathrm{R}\,-1} \quad (3a)$$

Voigt bound (isotropic strain): $$K_0^{\mathrm{V}} = \sum_i \left(c_{i10} + c_{i20} + c_{i30}\right)/9 = \sum_i k_{i0}^{\mathrm{V}}/9 \quad (3b)$$

To evaluate which stress state, hydrostatic stress or isotropic strain, better reflects the conditions inside the DAC for the setup used in our experiments, we calculated the Reuss and Voigt bound from the linear moduli k_{i0} obtained from our analysis of anisotropic compression and compared them with the bulk modulus K_0 obtained from our volume compression data. Using the linear BM-3 EOS parameters given in Table 3, we obtain $K_0^{\mathrm{R}} = 1/\sum_i k_{i0}^{-1} = 166.7(12)$ GPa (Equation 3a) and $K_0^{\mathrm{V}} = \sum_i k_{i0}/9 = 172.3(12)$ GPa (Equation 3b). The fact that the bulk modulus obtained by fitting the *P*-*V* data with a BM-3 EOS is virtually identical to the Reuss bound (Table 3) and coincides with the individual bulk moduli for the two crystals attests to the

quasi-hydrostatic stress field inside the pressure chamber of the DAC. For the explored pressure range, deviatoric stresses remained too weak to affect the compression behavior.

Equation of state of wadsleyite solid solutions

Available compression and elasticity data on wadsleyite solid solutions cover compositions spanned by four end members: Mg_2SiO_4 (mgwa), Fe_2SiO_4 (fewa), MgH_2SiO_4 (hywa), and $Fe^{2+}Fe^{3+}{}_2O_4$ (fe3wa). In defining these end members, we assumed that hydrogen incorporation is charge balanced by vacancies on the octahedral sites (Inoue 1994; Smyth 1994; Inoue et al. 1995; Kawamoto et al. 1996; Kudoh et al. 1996; Smyth et al. 1997; Litasov et al. 2011), i.e. by the mechanism $M_{M^x} + O_{O^x} + H_2O = V_M'' + 2\ (OH)_{O^\cdot} + MO$, and that ferric iron enters both the octahedral and tetrahedral sites by the charge coupled substitution $M_{M^x} + Si_{Si^x} + Fe_2O_3 = Fe_{M^\cdot} + Fe_{Si}' + MO + SiO_2$ (Woodland and Angel 1998; Richmond and Brodholt 2000; Frost and McCammon 2009), where M stands for Mg^{2+} or Fe^{2+} in octahedral coordination. Although alternative mechanisms to incorporate hydrogen, ferric iron, or coupled substitutions involving both of them have been proposed (Nishihara et al. 2008; Frost and McCammon 2009; Bolfan-Casanova et al. 2012; Smyth et al. 2014; Kawazoe et al. 2016), the chosen end members comprise the relevant chemical variability.

We can write a general wadsleyite formula as $(Mg,Fe^{2+},Fe^{3+})_{2-y}H_{2y}(Si,Fe^{3+})O_4$ where y stands for the number of H_2O molecular equivalents per formula unit. The iron content is conventionally stated as the ratio x = Fe/(Mg+Fe) without differentiating between iron oxidation states ($Fe = Fe^{2+} + Fe^{3+}$) and the ferric iron content as $z = Fe^{3+}/\sum Fe$. The following relations decompose a given wadsleyite formula into molar fractions x_m of the end members m:

Mg_2SiO_4 (mgwa): $$x_{\mathrm{mgwa}} = (1 - y/2)(1 - x(2 - z)/(2 - xz)) - y/2 \quad (4a)$$

Fe_2SiO_4 (fewa): $$x_{\text{fewa}} = (1 - y/2)x(2 - 3z)/(2 - xz) \quad (4b)$$

MgH_2SiO_4 (hywa): $$x_{\text{hywa}} = y \quad (4c)$$

Fe_3O_4 (fe3wa): $$x_{\text{fe3wa}} = (1 - y/2)2xz/(2 - xz) \quad (4d)$$

For each end member species *m*, the EOS parameters may have different values referred to as V_{0m}, K_{0m}, and K_{0m}'. Assuming ideal mixing behavior, the unit cell volume of wadsleyite solid solution members can be expressed as a function of the respective molar fractions

$$V = \sum_m x_m V_m = x_{\text{mgwa}} V_{\text{mgwa}} + x_{\text{fewa}} V_{\text{fewa}} + x_{\text{hywa}} V_{\text{hywa}} + x_{\text{fe3wa}} V_{\text{fe3wa}} \quad (5)$$

For wadsleyite solid solutions, ideal volumes of mixing have been observed for the dry system ($y = 0$) (Finger et al. 1993; Woodland et al. 2012), and the unit cell volume was found to be a linear function of the hydrogen concentration (Holl et al. 2008; Chang et al. 2015).

In Table S4[1], we compile published unit cell parameters for wadsleyites with different compositions. This dataset can be complemented by unit cell parameters for magnesium-free (Woodland and Angel 2000) and magnesium-bearing (Woodland et al. 2012) members of the spinelloid III solid solution series to cover the relevant composition space in the Mg_2SiO_4-Fe_2SiO_4-MgH_2SiO_4-Fe_3O_4 system (Figure 2). A least squares fit of Equation 5 to 72 unit cell volumes yields $V_{\text{mgwa }0}$ = 538.5(2) Å^3, $V_{\text{fewa }0}$ = 569.6(3) Å^3, $V_{\text{hywa }0}$ = 547.5(19) Å^3, and $V_{\text{fe3wa }0}$ = 598.5(5) Å^3 (Table 4). These unit cell volumes agree very well with previous estimates from solid solution analyses (Holl et al. 2008; Stixrude and Lithgow-Bertelloni 2011; Woodland et al. 2012; Chang et al. 2015). For example, the unit cell volume obtained for the fictive hydrous end member MgH_2SiO_4 (15.2 wt% H_2O) falls in between the values estimated using the formulas given by Holl et al. (2008) and Chang et al. (2015), i.e. 553.1(8) Å^3 and 547.4(31) Å^3, respectively.

To calculate the elastic moduli of wadsleyite solid solutions, we follow previous approaches to analyze the elastic properties of solid solutions (Takahashi and Liu 1970; Jackson et al. 1978; Stixrude and Lithgow-Bertelloni 2005) that are based on the Reuss average for the elastic properties of multi-phase aggregates. The elastic modulus M of a solid solution can then be calculated from the elastic moduli M_m, the molar fractions x_m, and the unit cell volumes V_m of the relevant end members (Hill 1963; Watt et al. 1976):

$$M^{\mathrm{R}} = \frac{\sum_m x_m V_m}{\sum_m x_m V_m / M_m} \quad (6)$$

Alternatively, the elastic modulus of a solid solution can be calculated from the end member moduli as a Voigt average (Hill 1963; Watt et al. 1976):

$$M^{\mathrm{V}} = \frac{\sum_m x_m V_m M_m}{\sum_m x_m V_m} \quad (7)$$

The choice between the two models depends on whether a single crystal of the solid solution is characterized by a homogeneous internal stress field (Reuss model) or is internally homogeneously strained (Voigt model). Note that Equations 6 and 7 average over end members or phases with different elastic properties while Equation 3 gives directional averages of elastic anisotropy for a single crystal.

To generate a set of comparable EOS for wadsleyites with different chemical compositions, we reanalyzed available room temperature compression data (Figure S7[1]). Since much of this data is limited to pressures below 10 GPa, we restricted our analysis of volume and axial compression curves to second-order Birch-Murnaghan (BM-2) EOS (Equations 1 and 2). The set of isothermal bulk and linear moduli can be complemented by adiabatic moduli determined with dynamic methods such as Brillouin spectroscopy, ultrasonic interferometry, and

resonant ultrasound spectroscopy by converting adiabatic moduli to isothermal moduli. The resulting dataset is compiled in Table 5 together with the respective references. Details about the procedures to reanalyze and convert previously published EOS and elasticity data can be found in the supplemental online material[1].

Figure 2 projects the wadsleyite compositions listed in Table 5 into ternary diagrams. Each ternary represents a projection from either the Fe_3O_4 end member (Figure 2a) or the MgH_2SiO_4 end member (Figure 2b) onto the opposite face of a fictitious tetrahedron spanned by the four end members at the corners. The compositions reported in previous EOS and elasticity studies cluster around the Mg_2SiO_4 end member and along the binary branches Mg_2SiO_4-Fe_2SiO_4 and Mg_2SiO_4-MgH_2SiO_4. Including that of the present study, only few compositions represent complex solid solutions that plot within the wadsleyite fields shown in Figure 2 rather than on the binary axes of the diagram. The wadsleyite fields cover the relevant compositional space as inferred from the reported maximum values $x_{\mathrm{hywa}} = 0.25$ (Smyth 1994; Inoue et al. 1995) and $x_{\mathrm{fewa}} = 0.3$ (Akaogi et al. 1989; Frost 2003; Stixrude and Lithgow-Bertelloni 2011) for wadsleyite solid solutions.

We derived end member bulk moduli K_m by fitting Equations 6 and 7 to the bulk moduli reported for different compositions (Table 5) and using the end member unit cell volumes V_m given in Table 4. We used the Reuss bounds for bulk and linear moduli as calculated from single-crystal elastic constants that were determined by Brillouin spectroscopy and employed the BM-2 bulk and linear moduli from compression curves for which the bulk modulus K_0 obtained from volume compression is close to the Reuss bound K_0^{R} calculated from the linear moduli (Equation 3, Table 5). Results reused in successive studies (Sinogeikin et al. 1998; Wang et al. 2014) were included only once. We found that both Reuss and Voigt models describe the wadsleyite bulk and linear moduli equally well and, within errors, give identical results for intermediate compositions

as well as for end members. The moduli for the hydrous end member MgH_2SiO_4 are the only exceptions with the Voigt model moduli being significantly smaller than the Reuss model moduli (Tables 4 and S5[1]). Since both models predict virtually identical moduli for intermediate compositions, we focus the following discussion on the Reuss model for clarity.

Table 4 lists the results of least squares fits of Equation 6 (Reuss model) to 21 compositions and the corresponding bulk and linear moduli for the ternary system Mg_2SiO_4-Fe_2SiO_4-MgH_2SiO_4. The resulting bulk modulus for the Mg_2SiO_4 end member agrees with those reported in previous solid solution analyses (Jeanloz and Hazen 1991; Holl et al. 2008; Mao et al. 2008b; Stixrude and Lithgow-Bertelloni 2011; Chang et al. 2015; Mao and Li 2016). The incorporation of hydrogen into wadsleyite reduces the bulk modulus as reported in earlier studies (Holl et al. 2008; Mao et al. 2008b; Tsuchiya and Tsuchiya 2009; Ye et al. 2010; Mao et al. 2011; Chang et al. 2015; Mao and Li 2016). Moreover, hydrogen weakens the structure along all three crystallographic axes with the strongest reduction of the linear modulus along **b** (Table 4).

The compression behavior of the Mg_2SiO_4-Fe_2SiO_4 solid solution is not tightly constrained by the available studies. As a result, the bulk modulus for the ferrous iron-bearing end member Fe_2SiO_4 has large uncertainties. In contrast to earlier studies concluding that iron has a small or negligible effect on the bulk modulus (Stixrude and Lithgow-Bertelloni 2011; Wang et al. 2014; Chang et al. 2015; Mao and Li 2016), however, the combination of our new data with a careful reanalysis of previous studies indicates that the substitution of Mg^{2+} by Fe^{2+} increases the incompressibility of wadsleyite by about 14 %. Ferrous iron appears to stiffen the crystal structure along all three crystallographic axes with the strongest stiffening along **a** (Table 4).

A similar increase in bulk modulus with iron content has been observed for ringwoodite (Rigden and Jackson 1991; Jackson et al. 2000; Higo et al. 2006) and olivine (Sumino 1979; Zha et al. 1996; Speziale et al. 2004). These experimental observations are consistent with first-

principle calculations based on density functional theory (DFT) suggesting that the bulk moduli increase with increasing iron content for all three $(Mg,Fe)_2SiO_4$ polymorphs (Núñez-Valdez et al. 2011, 2013). In the case of wadsleyite, the DFT calculations predict the absolute difference in bulk modulus between the magnesium and iron end members to be 22 GPa (Núñez-Valdez et al. 2011) and 42 GPa (Núñez-Valdez et al. 2013). These values are similar in magnitude to the difference of 25 GPa observed in our analysis.

For the quaternary system Mg_2SiO_4-Fe_2SiO_4-MgH_2SiO_4-Fe_3O_4, we also included the moduli for the member of the spinelloid III solid solution (Hazen et al. 2000b). The effect of Fe^{3+} is weakly constrained leading to large uncertainties on the moduli for the iron-bearing end members (Table 4). However, the trends observed for the ternary system remained unchanged. In contrast to the stiffening of the crystal structure by ferrous iron, ferric iron appears to soften the crystal structure on compression, especially along the **a** axis (Table 4). This behavior differs from the situation in the spinel-structured solid solution, in which the bulk moduli for magnetite (186 GPa, Finger et al. 1986; Reichmann and Jacobsen 2004) and for Mg_2SiO_4 ringwoodite (185 GPa, Jackson et al. 2000; Higo et al. 2006) are essentially identical.

Most iron-bearing wadsleyites can be expected to contain some ferric iron (O'Neill et al. 1993; McCammon et al. 2004; Frost and McCammon 2009; Bolfan-Casanova et al. 2012) even though the amount of ferric iron has not always been stated for the samples described in the literature. The competing effects of ferrous and ferric iron on the volume and anisotropic compression of wadsleyite could have masked each other in previous attempts to resolve the effect of iron-magnesium substitution on the compression behavior compelling to conclude this effect to be negligible for wadsleyite (Wang et al. 2014; Chang et al. 2015; Mao and Li 2016).

The bulk moduli compiled in Table 5 are plotted as a function of Fe/(Mg+Fe) and the number of H_2O molecular equivalents in Figures 3a and 3b, respectively (for linear moduli see

Figure S8[1]). For each composition listed in Table 5, the modulus as calculated from the end member models (Table 4) is shown for comparison. The models reasonably capture the competing effects arising from the different cation substitutions even though several experimental data clearly deviate from the calculated values. Deviations may arise from the presence of hydrogen and ferric iron, whose concentrations have not been accurately determined in several studies, or from systematic errors in the compression studies. For example, the bulk moduli in excess of 180 GPa at Fe/(Mg+Fe) ratios of 0 and 0.25 (Figure 3a, Table 5) were both obtained from refitting the compression data of Hazen et al. (2000a). Even though the bulk modulus values are much larger than any other values obtained from compression data, they still display the trend of increasing bulk moduli with increasing Fe/(Mg+Fe) ratio. Moreover, both data points have counterparts with fairly low bulk modulus values for identical compositions (Figure 3a, Table 5, Hazen et al. (1990)) that again follow the trend of our model.

Relationship of compression behavior to crystal chemistry

In the wadsleyite crystal structure, iron preferentially enters the M3 and M1 octahedral sites (Sawamoto and Horiuchi 1990; Finger et al. 1993; Hazen et al. 2000a). While the M3 octahedra form edge-sharing double chains along the **a** axis, the M1 octahedra interconnect these chains along the **c** axis by sharing edges with octahedra belonging to two double chains. In contrast to bulk modulus-volume systematics for coordination polyhedra (Hazen and Finger 1979), the M1 and M3 octahedra stiffen along with the expansion arising from the replacement of Mg^{2+} by the larger Fe^{2+} cation (Finger et al. 1993; Hazen et al. 2000a). As a consequence, we found that the wadsleyite crystal structure becomes less compressible when Mg^{2+} is replaced by Fe^{2+}. The stiffening of coordination polyhedra by incorporation of iron may be caused by

444 geometrical constraints imposed by the rigid sorosilicate group (Hazen et al. 2000a) in addition to
445 changes in the chemical bonding character.

446 For ringwoodite, the increase of the bulk modulus with iron content has been related to *d*
447 electron interactions between iron cations occupying edge-sharing coordination octahedra (Hazen
448 1993). Indeed, *d* electron interactions have been observed for both iron-bearing ringwoodite and
449 wadsleyite in the form of $Fe^{2+} \rightarrow Fe^{3+}$ intervalence charge transfer between edge-sharing
450 octahedra by Mössbauer spectroscopy (McCammon et al. 2004; Mrosko et al. 2015) and optical
451 absorption spectroscopy (Ross 1997; Keppler and Smyth 2005). The fact that Mg-Fe solid
452 solutions of both ringwoodite and wadsleyite appear to contradict bulk modulus-volume
453 systematics, which are essentially based on ionic bonding models (Anderson and Anderson 1970;
454 Chung 1972), suggests a change in bonding character and crystal-chemical behavior of the Fe^{2+}
455 cation at high pressure (Hazen 1993).

456 Required to charge balance structurally bound hydroxyl groups in wadsleyite (Smyth
457 1994; Inoue et al. 1995; Kudoh et al. 1996; Smyth et al. 1997; Demouchy et al. 2005; Jacobsen et
458 al. 2005; Litasov et al. 2011), octahedral vacancies are probably responsible for the enhanced
459 compressibility of the wadsleyite structure with increasing degree of hydration (Holl et al. 2008;
460 Tsuchiya and Tsuchiya 2009; Ye et al. 2010). On one hand, octahedral vacancies disrupt the
461 polyhedral framework of the crystal structure and allow the structure to relax into the created
462 voids. On the other hand, hydroxyl groups and accompanying hydrogen bonds counteract the
463 repulsive forces between neighboring oxygen anions (Kleppe et al. 2001, 2006; Jacobsen et al.
464 2005). Both vacancies and hydrogen bonds can therefore be expected to reduce the bulk modulus
465 of wadsleyite.

466 The incorporation of Fe^{3+} into the wadsleyite structure follows a coupled substitution with
467 Si^{4+} and M^{2+} ($M^{2+} = Mg^{2+}$ or Fe^{2+}) being replaced by two Fe^{3+}, one at an tetrahedral and one at an

468 octahedral site (Woodland and Angel 1998; Richmond and Brodholt 2000). The presence of
469 ferric iron in the tetrahedron was confirmed by the single-crystal X-ray diffraction study of
470 Smyth et al. (2014). However, using chemical compositional trends, Frost and McCammon
471 (2009) showed that a substantial fraction of the ferric iron substitutes for octahedral cations only,
472 following the reaction 3 M_{M^x} + Fe_2O_3 = 2 $Fe_{M^\cdot}$ + V_M'' + 3 MO with M = Mg^{2+} or Fe^{2+}. The
473 created vacancies V_M'' will enhance the compressibility with respect to the Mg_2SiO_4 end member
474 as might be reflected in the low value estimated for the bulk modulus of the Fe_3O_4 end member
475 (Table 4).
476
477 **Bulk modulus systematics**
478 We visualize the variation of volume and bulk modulus across the wadsleyite solid
479 solutions using a diagram relating the product of the bulk modulus K and the mean atomic
480 volume V_A, KV_A, to the mean atomic mass M_A (Chung 1972), where $V_A = V/(ZN)$ and $M_A = M/N$
481 with the unit cell volume V, the formula mass M, the number of formula units per unit cell Z, and
482 the number of atoms per formula N. Based on a theoretical model for ionic bonding and an
483 empirical analysis of isostructural compounds, the product KV_A was shown to remain constant for
484 isostructural and isovalent exchange, i.e. when cations of equal charges substitute in the same
485 crystal structure (Anderson and Anderson 1970; Chung 1972).
486 In Figure 4, we plot the data of Table 5 together with the trends calculated using the 4-end
487 member EOS model (Equations 4, 5, and 6, Table 4) into a KV_A-M_A diagram. In cases where unit
488 cell volumes are not reported in the original publications, we calculated unit cell volumes
489 according to our model. The M_A axis splits up the trends of iron-magnesium substitution and
490 hydration since they increase or decrease the mean atomic mass, respectively. In general, the
491 experimental data follow the trends predicted by the EOS model. In addition to measurement

492 uncertainties, scatter results from solid solutions in the ternary or quaternary system that should
493 fall between the lines calculated for the binary systems.

494 From a purely ionic perspective, replacing Mg^{2+} by Fe^{2+} should spread the data along a
495 horizontal line of constant KV_A extending from the Mg_2SiO_4 end member towards higher mean
496 atomic masses. Based on the EOS model, however, the product KV_A increases with increasing
497 ferrous iron content, supporting the conclusion above that an assumption of purely ionic bonding
498 is not valid for iron-bearing wadsleyites. A change in bonding character away from
499 predominantly ionic Mg–O bonds in Mg_2SiO_4 towards an increasing contribution of more
500 covalent Fe^{2+}–O bonds, on the other hand, may explain the deviation from constant KV_A. The
501 incorporation of Fe^{3+}, in contrast, decreases the product KV_A. Most of the data plot between the
502 two opposing trends further suggesting that ferric iron is present in many wadsleyite samples.

503 In the case of hydration, both experimental data and the EOS model define a clear trend
504 towards lower products KV_A with decreasing mean atomic mass. The steep slope of this trend
505 again contradicts the simple picture of ionic bonding and isostructural cation exchange. In
506 wadsleyite, hydration goes along with creation of vacancies (Smyth 1994; Inoue et al. 1995;
507 Kudoh et al. 1996) and formation of hydrogen bonds (Kleppe et al. 2001, 2006). Exchanging a
508 divalent octahedral cation for two protons results in local structural rearrangements (Jacobsen et
509 al. 2005; Tsuchiya and Tsuchiya 2009; Deon et al. 2010; Griffin et al. 2013). These fundamental
510 rearrangements are not captured by a simple ionic model based on isostructural cation exchange.

511 In addition to the wadsleyite data, Figure 4 includes information about the $(Mg,Fe)_2SiO_4$
512 polymorphs olivine and ringwoodite. For these structures, the magnesian and ferrous end
513 members exist as stable compounds, and their properties can be measured directly. For both
514 polymorphs, the product KV_A increases with increasing Fe^{2+} content, and the differences between
515 the two end members are similar to the difference calculated using our EOS model for

516 wadsleyite. This parallelism between the $(Mg,Fe)_2SiO_4$ polymorphs not only points to the
517 importance of covalent bonding in mineral structures but also supports the validity of our multi-
518 end member EOS model for wadsleyite solid solutions.
519
520 **Implications**
521 Contradicting previous inferences (Wang et al. 2014; Chang et al. 2015; Mao and Li
522 2016), the combination of our new data with a careful reanalysis of previously published work
523 suggests that the incorporation of ferrous iron into wadsleyite increases its bulk modulus. In
524 many mantle minerals including the $(Mg,Fe)_2SiO_4$ polymorphs and ferropericlase, (Mg,Fe)O, as
525 an adequate standard material for the behavior of M–O bonds (M = Mg^{2+}, Fe^{2+}), substitution of
526 Mg^{2+} by Fe^{2+} stiffens the crystal structure (Jackson et al. 1978; Hazen 1993; Stixrude and
527 Lithgow-Bertelloni 2011) in response to the related gain in covalent bonding. These findings are
528 important for the modelling of seismic wave velocities in potentially iron-enriched mantle
529 regions in Earth's transition zone. Since the Martian mantle likely contains at least twice the
530 amount of iron as compared to Earth's mantle (McGetchin and Smith 1978), our model for
531 wadsleyite $(Mg,Fe)_2SiO_4$ solid solutions will also facilitate the interpretation of future seismic
532 data of the deep Martian mantle provided by the InSight space mission.
533 For example, the bulk sound velocity $v_\phi = (KV_A/M_A)^{1/2}$ can be directly obtained from our
534 model neglecting the small (~ 1 %) isothermal to adiabatic conversion for the bulk modulus. The
535 contours in Figure 4 show lines of constant bulk sound velocity. Changing the wadsleyite
536 composition away from pure Mg_2SiO_4 and along the trends between the end members reduces the
537 bulk sound velocity as contour lines are crossed. Increasing pressure to 15 GPa shifts the trends
538 between the end members of our model (dotted lines in Figure 4) to higher bulk sound velocities.
539 However, the mutual differences in bulk sound velocity among the end members are retained

with Mg_2SiO_4 being the fastest and Fe_3O_4 the slowest. This conclusion, however, only holds for $K_0' = 4$ for every end member. Our *P-V* data clearly show that $K_0' > 4$ for iron-bearing wadsleyite (Table 3) while the values for K_0' reported in the literature not only cover a wide range but also contradict each other for specific compositions (Mao et al. 2011; Chang et al. 2015). Future studies are needed to accurately determine the pressure derivative of the bulk modulus and to clarify whether changes in composition may lead to velocity crossovers for specific wadsleyite compositions at high pressures as observed for forsterite (Mao et al. 2010).

Acknowledgments

We thank A. Potzel and D. Krause for electron microprobe analyses and R. Njul and H. Schulze for polishing the crystal sections. This research was supported through the project "GeoMaX", funded under the Emmy-Noether Program of the German Science Foundation (MA4534/3-1). H. M. acknowledges support from the Bavarian Academy of Sciences. The FEI Scios DualBeam machine at the Bayerisches Geoinstitut (University of Bayreuth) was supported by the German Science Foundation under Grant INST 91/315-1 FUGG.

References cited

Agee, C.B. (1998) Phase transformations and seismic structure in the upper mantle and transition zone. Reviews in Mineralogy, 37, 165–203.

Akaogi, M., Ito, E., and Navrotsky, A. (1989) Olivine-modified spinel-spinel transitions in the system Mg_2SiO_4-Fe_2SiO_4: Calorimetric measurements, thermochemical calculation, and geophysical application. Journal of Geophysical Research: Solid Earth, 94, 15671–15685.

562 Anderson, D.L., and Anderson, O.L. (1970) The bulk modulus-volume relationship for oxides.
563 Journal of Geophysical Research, 75, 3494–3500.

564 Angel, R.J. (2000) Equations of State. Reviews in Mineralogy and Geochemistry, 41, 35–59.

565 ——— (2003) Automated profile analysis for single-crystal diffraction data. Journal of Applied
566 Crystallography, 36, 295–300.

567 Angel, R.J., and Finger, L.W. (2011) *SINGLE*: a program to control single-crystal
568 diffractometers. Journal of Applied Crystallography, 44, 247–251.

569 Angel, R.J., Alvaro, M., and Gonzalez-Platas, J. (2014) EosFit7c and a Fortran module (library)
570 for equation of state calculations. Zeitschrift für Kristallographie - Crystalline Materials,
571 229, 405–419.

572 Bina, C.R., and Wood, B.J. (1987) Olivine-spinel transitions: Experimental and thermodynamic
573 constraints and implications for the nature of the 400-km seismic discontinuity. Journal of
574 Geophysical Research: Solid Earth, 92, 4853–4866.

575 Birch, F. (1947) Finite Elastic Strain of Cubic Crystals. Physical Review, 71, 809–824.

576 Bolfan-Casanova, N., Muñoz, M., McCammon, C., Deloule, E., Férot, A., Demouchy, S., France,
577 L., Andrault, D., and Pascarelli, S. (2012) Ferric iron and water incorporation in
578 wadsleyite under hydrous and oxidizing conditions: A XANES, Mössbauer, and SIMS
579 study. American Mineralogist, 97, 1483–1493.

580 Chang, Y.-Y., Jacobsen, S.D., Bina, C.R., Thomas, S.-M., Smyth, J.R., Frost, D.J., Boffa
581 Ballaran, T., McCammon, C.A., Hauri, E.H., Inoue, T., and others (2015) Comparative
582 compressibility of hydrous wadsleyite and ringwoodite: Effect of H_2O and implications

583 for detecting water in the transition zone. Journal of Geophysical Research: Solid Earth,
584 120, 8259–8280.

585 Chung, D.H. (1972) Birch's law: Why is it so good? Science, 177, 261–263.

586 Demouchy, S., Deloule, E., Frost, D.J., and Keppler, H. (2005) Pressure and temperature-
587 dependence of water solubility in Fe-free wadsleyite. American Mineralogist, 90, 1084–
588 1091.

589 Deon, F., Koch-Müller, M., Rhede, D., Gottschalk, M., Wirth, R., and Thomas, S.-M. (2010)
590 Location and quantification of hydroxyl in wadsleyite: New insights. American
591 Mineralogist, 95, 312–322.

592 Fei, Y., Mao, H., Shu, J., Parthasarathy, G., Bassett, W.A., and Ko, J. (1992) Simultaneous high-
593 *P*, high-*T* X ray diffraction study of β-$(Mg,Fe)_2SiO_4$ to 26 GPa and 900 K. Journal of
594 Geophysical Research: Solid Earth, 97, 4489–4495.

595 Finger, L.W., Hazen, R.M., and Hofmeister, A.M. (1986) High-pressure crystal chemistry of
596 spinel ($MgAl_2O_4$) and magnetite (Fe_3O_4): Comparisons with silicate spinels. Physics and
597 Chemistry of Minerals, 13, 215–220.

598 Finger, L.W., Hazen, R.M., Zhang, J., Ko, J., and Navrotsky, A. (1993) The effect of Fe on the
599 crystal structure of wadsleyite β-$(Mg_{1-x}Fe_x)_2SiO_4$, $0.00 \leq x \leq 0.40$. Physics and Chemistry of
600 Minerals, 19, 361–368.

601 Frost, D.J. (2003) The structure and sharpness of $(Mg,Fe)_2SiO_4$ phase transformations in the
602 transition zone. Earth and Planetary Science Letters, 216, 313–328.

603 ——— (2008) The upper mantle and transition zone. Elements, 4, 171–176.

Frost, D.J., and Dolejš, D. (2007) Experimental determination of the effect of H_2O on the 410-km seismic discontinuity. Earth and Planetary Science Letters, 256, 182–195.

Frost, D.J., and McCammon, C.A. (2009) The effect of oxygen fugacity on the olivine to wadsleyite transformation: Implications for remote sensing of mantle redox state at the 410 km seismic discontinuity. American Mineralogist, 94, 872–882.

Fujisawa, H. (1998) Elastic wave velocities of forsterite and its β-spinel form and chemical boundary hypothesis for the 410-km discontinuity. Journal of Geophysical Research: Solid Earth, 103, 9591–9608.

Griffin, J.M., Berry, A.J., Frost, D.J., Wimperis, S., and Ashbrook, S.E. (2013) Water in the Earth's mantle: a solid-state NMR study of hydrous wadsleyite. Chemical Science, 4, 1523–1538.

Haussühl, S. (2007) Physical Properties of Crystals: An Introduction, 453 p. Wiley-VCH, Weinheim.

Hazen, R.M. (1993) Comparative compressibilities of silicate spinels: Anomalous behavior of $(Mg,Fe)_2SiO_4$. Science, 259, 206–209.

Hazen, R.M., and Finger, L.W. (1979) Bulk modulus—volume relationship for cation-anion polyhedra. Journal of Geophysical Research: Solid Earth, 84, 6723–6728.

Hazen, R.M., Zhang, J., and Ko, J. (1990) Effects of Fe/Mg on the compressibility of synthetic wadsleyite: β-$(Mg_{1-x}Fe_x)_2SiO_4$ ($x \leq 0.25$). Physics and Chemistry of Minerals, 17, 416–419.

623 Hazen, R.M., Weinberger, M.B., Yang, H., and Prewitt, C.T. (2000a) Comparative high-pressure
624 crystal chemistry of wadsleyite, β-$(Mg_{1-x}Fe_x)_2SiO_4$, with $x = 0$ and 0.25. American
625 Mineralogist, 85, 770–777.

626 Hazen, R.M., Yang, H., and Prewitt, C.T. (2000b) High-pressure crystal chemistry of Fe^{3+}-
627 wadsleyite, β-$Fe_{2.33}Si_{0.67}O_4$. American Mineralogist, 85, 778–783.

628 Higo, Y., Inoue, T., Li, B., Irifune, T., and Liebermann, R.C. (2006) The effect of iron on the
629 elastic properties of ringwoodite at high pressure. Physics of the Earth and Planetary
630 Interiors, 159, 276–285.

631 Hill, R. (1963) Elastic properties of reinforced solids: Some theoretical principles. Journal of the
632 Mechanics and Physics of Solids, 11, 357–372.

633 Holl, C.M., Smyth, J.R., Jacobsen, S.D., and Frost, D.J. (2008) Effects of hydration on the
634 structure and compressibility of wadsleyite, β-(Mg_2SiO_4). American Mineralogist, 93,
635 598–607.

636 Horiuchi, H., and Sawamoto, H. (1981) *β*-Mg_2SiO_4: Single-crystal X-ray diffraction study.
637 American Mineralogist, 66, 568–575.

638 Houser, C. (2016) Global seismic data reveal little water in the mantle transition zone. Earth and
639 Planetary Science Letters, 448, 94–101.

640 Inoue, T. (1994) Effect of water on melting phase relations and melt composition in the system
641 Mg_2SiO_4–$MgSiO_3$–H_2O up to 15 GPa. Physics of the Earth and Planetary Interiors, 85,
642 237–263.

643 Inoue, T., Yurimoto, H., and Kudoh, Y. (1995) Hydrous modified spinel, $Mg_{1.75}SiH_{0.5}O_4$: A new
644 water reservoir in the mantle transition region. Geophysical Research Letters, 22, 117–
645 120.

646 Isaak, D.G., Anderson, O.L., Goto, T., and Suzuki, I. (1989) Elasticity of single-crystal forsterite
647 measured to 1700 K. Journal of Geophysical Research: Solid Earth, 94, 5895–5906.

648 Isaak, D.G., Gwanmesia, G.D., Falde, D., Davis, M.G., Triplett, R.S., and Wang, L. (2007) The
649 elastic properties of β-Mg_2SiO_4 from 295 to 660 K and implications on the composition of
650 Earth's upper mantle. Physics of the Earth and Planetary Interiors, 162, 22–31.

651 Isaak, D.G., Gwanmesia, G.D., Davis, M.G., Stafford, S.C., Stafford, A.M., and Triplett, R.S.
652 (2010) The temperature dependence of the elasticity of Fe-bearing wadsleyite. Physics of
653 the Earth and Planetary Interiors, 182, 107–112.

654 Jackson, I., Liebermann, R.C., and Ringwood, A.E. (1978) The elastic properties of $(Mg_xFe_{1-x})O$
655 solid solutions. Physics and Chemistry of Minerals, 3, 11–31.

656 Jackson, J.M., Sinogeikin, S.V., and Bass, J.D. (2000) Sound velocities and elastic properties of
657 γ-Mg_2SiO_4 to 873 K by Brillouin spectroscopy. American Mineralogist, 85, 296–303.

658 Jacobsen, S.D., Demouchy, S., Frost, D.J., Ballaran, T.B., and Kung, J. (2005) A systematic
659 study of OH in hydrous wadsleyite from polarized FTIR spectroscopy and single-crystal
660 X-ray diffraction: Oxygen sites for hydrogen storage in Earth's interior. American
661 Mineralogist, 90, 61–70.

Jeanloz, R., and Hazen, R.M. (1991) Finite-strain analysis of relative compressibilities: Application to the high-pressure wadsleyite phase as an illustration. American Mineralogist, 76, 1765–1768.

Kantor, I., Prakapenka, V., Kantor, A., Dera, P., Kurnosov, A., Sinogeikin, S., Dubrovinskaia, N., and Dubrovinsky, L. (2012) BX90: A new diamond anvil cell design for X-ray diffraction and optical measurements. Review of Scientific Instruments, 83, 125102.

Katsura, T., Mayama, N., Shouno, K., Sakai, M., Yoneda, A., and Suzuki, I. (2001) Temperature derivatives of elastic moduli of $(Mg_{0.91}Fe_{0.09})_2SiO_4$ modified spinel. Physics of the Earth and Planetary Interiors, 124, 163–166.

Katsura, T., Yoneda, A., Yamazaki, D., Yoshino, T., and Ito, E. (2010) Adiabatic temperature profile in the mantle. Physics of the Earth and Planetary Interiors, 183, 212–218.

Kawamoto, T., Hervig, R.L., and Holloway, J.R. (1996) Experimental evidence for a hydrous transition zone in the early Earth's mantle. Earth and Planetary Science Letters, 142, 587–592.

Kawazoe, T., Buchen, J., and Marquardt, H. (2015) Synthesis of large wadsleyite single crystals by solid-state recrystallization. American Mineralogist, 100, 2336–2339.

Kawazoe, T., Chaudhari, A., Smyth, J.R., and McCammon, C. (2016) Coupled substitution of Fe^{3+} and H^+ for Si in wadsleyite: A study by polarized infrared and Mössbauer spectroscopies and single-crystal X-ray diffraction. American Mineralogist, 101, 1236–1239.

Keppler, H., and Smyth, J.R. (2005) Optical and near infrared spectra of ringwoodite to 21.5 GPa: Implications for radiative heat transport in the mantle. American Mineralogist, 90, 1209–1212.

King, H.E., and Finger, L.W. (1979) Diffracted beam crystal centering and its application to high-pressure crystallography. Journal of Applied Crystallography, 12, 374–378.

Kleppe, A.K., Jephcoat, A.P., Olijnyk, H., Slesinger, A.E., Kohn, S.C., and Wood, B.J. (2001) Raman spectroscopic study of hydrous wadsleyite (β-Mg_2SiO_4) to 50 GPa. Physics and Chemistry of Minerals, 28, 232–241.

Kleppe, A.K., Jephcoat, A.P., and Smyth, J.R. (2006) High-pressure Raman spectroscopic study of Fo_{90} hydrous wadsleyite. Physics and Chemistry of Minerals, 32, 700–709.

Klotz, S., Chervin, J.-C., Munsch, P., and Marchand, G.L. (2009) Hydrostatic limits of 11 pressure transmitting media. Journal of Physics D: Applied Physics, 42, 075413.

Koch, M., Woodland, A.B., and Angel, R.J. (2004) Stability of spinelloid phases in the system Mg_2SiO_4–Fe_2SiO_4–Fe_3O_4 at 1100 °C and up to 10.5 GPa. Physics of the Earth and Planetary Interiors, 143–144, 171–183.

Kudoh, Y., and Inoue, T. (1998) Effect of pressure on the crystal structure of hydrous wadsleyite, $Mg_{1.75}SiH_{0.5}O_4$. In M.H. Manghnani and T. Yagi, Eds., Properties of Earth and Planetary Materials at High Pressure and Temperature pp. 517–521. American Geophysical Union, Washington, DC.

Kudoh, Y., and Inoue, T. (1999) Mg-vacant structural modules and dilution of the symmetry of hydrous wadsleyite, β-$Mg_{2-x}SiH_{2x}O_4$ with $0.00 \leq x \leq 0.25$. Physics and Chemistry of Minerals, 26, 382–388.

Kudoh, Y., Inoue, T., and Arashi, H. (1996) Structure and crystal chemistry of hydrous wadsleyite, $Mg_{1.75}SiH_{0.5}O_4$: possible hydrous magnesium silicate in the mantle transition zone. Physics and Chemistry of Minerals, 23, 461–469.

Kurnosov, A., Kantor, I., Boffa-Ballaran, T., Lindhardt, S., Dubrovinsky, L., Kuznetsov, A., and Zehnder, B.H. (2008) A novel gas-loading system for mechanically closing of various types of diamond anvil cells. Review of Scientific Instruments, 79, 045110.

Li, B., and Liebermann, R.C. (2000) Sound velocities of wadsleyite β-$(Mg_{0.88}Fe_{0.12})_2SiO_4$ to 10 GPa. American Mineralogist, 85, 292–295.

Li, B., Gwanmesia, G.D., and Liebermann, R.C. (1996) Sound velocities of olivine and beta polymorphs of Mg_2SiO_4 at Earth's transition zone pressures. Geophysical Research Letters, 23, 2259–2262.

Li, B., Liebermann, R.C., and Weidner, D.J. (1998) Elastic moduli of wadsleyite (β-Mg_2SiO_4) to 7 gigapascals and 873 Kelvin. Science, 281, 675–677.

——— (2001) P-V-V_p-V_s-T measurements on wadsleyite to 7 GPa and 873 K: Implications for the 410-km seismic discontinuity. Journal of Geophysical Research: Solid Earth, 106, 30579–30591.

Libowitzky, E., and Rossman, G.R. (1996) Principles of quantitative absorbance measurements in anisotropic crystals. Physics and Chemistry of Minerals, 23, 319–327.

——— (1997) An IR absorption calibration for water in minerals. American Mineralogist, 82, 1111–1115.

Litasov, K.D., Shatskiy, A., Ohtani, E., and Katsura, T. (2011) Systematic study of hydrogen incorporation into Fe-free wadsleyite. Physics and Chemistry of Minerals, 38, 75–84.

Liu, W., Kung, J., Li, B., Nishiyama, N., and Wang, Y. (2009) Elasticity of $(Mg_{0.87}Fe_{0.13})_2SiO_4$ wadsleyite to 12 GPa and 1073 K. Physics of the Earth and Planetary Interiors, 174, 98–104.

Mao, Z., and Li, X. (2016) Effect of hydration on the elasticity of mantle minerals and its geophysical implications. Science China Earth Sciences, 59, 873–888.

Mao, Z., Jacobsen, S.D., Jiang, F., Smyth, J.R., Holl, C.M., and Duffy, T.S. (2008a) Elasticity of hydrous wadsleyite to 12 GPa: Implications for Earth's transition zone. Geophysical Research Letters, 35, L21305.

Mao, Z., Jacobsen, S.D., Jiang, F.M., Smyth, J.R., Holl, C.M., Frost, D.J., and Duffy, T.S. (2008b) Single-crystal elasticity of wadsleyites, β-Mg_2SiO_4, containing 0.37–1.66 wt.% H_2O. Earth and Planetary Science Letters, 268, 540–549.

Mao, Z., Jacobsen, S.D., Jiang, F., Smyth, J.R., Holl, C.M., Frost, D.J., and Duffy, T.S. (2010) Velocity crossover between hydrous and anhydrous forsterite at high pressures. Earth and Planetary Science Letters, 293, 250–258.

Mao, Z., Jacobsen, S.D., Frost, D.J., McCammon, C.A., Hauri, E.H., and Duffy, T.S. (2011) Effect of hydration on the single-crystal elasticity of Fe-bearing wadsleyite to 12 GPa. American Mineralogist, 96, 1606–1612.

743 Marquardt, H., and Marquardt, K. (2012) Focused ion beam preparation and characterization of
744 single-crystal samples for high-pressure experiments in the diamond-anvil cell. American
745 Mineralogist, 97, 299–304.

746 Mayama, N., Suzuki, I., Saito, T., Ohno, I., Katsura, T., and Yoneda, A. (2004) Temperature
747 dependence of elastic moduli of β-$(Mg, Fe)_2SiO_4$. Geophysical Research Letters, 31,
748 L04612.

749 McCammon, C.A., Frost, D.J., Smyth, J.R., Laustsen, H.M.S., Kawamoto, T., Ross, N.L., and
750 van Aken, P.A. (2004) Oxidation state of iron in hydrous mantle phases: implications for
751 subduction and mantle oxygen fugacity. Physics of the Earth and Planetary Interiors, 143–
752 144, 157–169.

753 McGetchin, T.R., and Smith, J.R. (1978) The mantle of Mars: Some possible geological
754 implications of its high density. Icarus, 34, 512–536.

755 McMillan, P.F., Akaogi, M., Sato, R.K., Poe, B., and Foley, J. (1991) Hydroxyl groups in *β*-
756 Mg_2SiO_4. American Mineralogist, 76, 354–360.

757 Meng, Y., Weidner, D.J., and Fei, Y. (1993) Deviatoric stress in a quasi-hydrostatic diamond
758 anvil cell: Effect on the volume-based pressure calibration. Geophysical Research Letters,
759 20, 1147–1150.

760 Mizukami, S., Ohtani, A., Kawai, N., and Ito, E. (1975) High-pressure X-ray diffraction studies
761 on *β*- and *γ*-Mg_2SiO_4. Physics of the Earth and Planetary Interiors, 10, 177–182.

762 Mrosko, M., Koch-Müller, M., McCammon, C., Rhede, D., Smyth, J.R., and Wirth, R. (2015)
763 Water, iron, redox environment: effects on the wadsleyite–ringwoodite phase transition.
764 Contributions to Mineralogy and Petrology, 170, 9.

765 Nishihara, Y., Shinmei, T., and Karato, S. (2008) Effect of chemical environment on the
766 hydrogen-related defect chemistry in wadsleyite. American Mineralogist, 93, 831–843.

767 Núñez-Valdez, M., da Silveira, P., and Wentzcovitch, R.M. (2011) Influence of iron on the
768 elastic properties of wadsleyite and ringwoodite. Journal of Geophysical Research: Solid
769 Earth, 116, B12207.

770 Núñez-Valdez, M., Wu, Z., Yu, Y.G., and Wentzcovitch, R.M. (2013) Thermal elasticity of
771 $(Fe_x,Mg_{1-x})_2SiO_4$ olivine and wadsleyite. Geophysical Research Letters, 40, 290–294.

772 Nye, J.F. (1985) Physical Properties of Crystals: Their Representation by Tensors and Matrices,
773 352 p. Oxford University Press, Oxford.

774 O'Neill, H.St.C., McCammon, C.A., Canil, D., Rubie, D.C., Ross, C.R.I., and Seifert, F. (1993)
775 Mössbauer spectroscopy of mantle transition zone phases and determination of minimum
776 Fe^{3+} content. American Mineralogist, 78, 456–460.

777 Paterson, M.S. (1982) The determination of hydroxyl by infrared absorption in quartz, silicate
778 glasses and similar materials. Bulletin de Minéralogie, 105, 20–29.

779 Prescher, C., McCammon, C., and Dubrovinsky, L. (2012) *MossA*: a program for analyzing
780 energy-domain Mössbauer spectra from conventional and synchrotron sources. Journal of
781 Applied Crystallography, 45, 329–331.

Reichmann, H.J., and Jacobsen, S.D. (2004) High-pressure elasticity of a natural magnetite crystal. American Mineralogist, 89, 1061–1066.

Reuss, A. (1929) Berechnung der Fließgrenze von Mischkristallen auf Grund der Plastizitätsbedingung für Einkristalle. Zeitschrift für Angewandte Mathematik und Mechanik, 9, 49–58 (in German).

Richmond, N.C., and Brodholt, J.P. (2000) Incorporation of Fe^{3+} into forsterite and wadsleyite. American Mineralogist, 85, 1155–1158.

Rigden, S.M., and Jackson, I. (1991) Elasticity of germanate and silicate spinels at high pressure. Journal of Geophysical Research: Solid Earth, 96, 9999–10006.

Ringwood, A.E. (1991) Phase transformations and their bearing on the constitution and dynamics of the mantle. Geochimica et Cosmochimica Acta, 55, 2083–2110.

Ringwood, A.E., and Major, A. (1970) The system Mg_2SiO_4-Fe_2SiO_4 at high pressures and temperatures. Physics of the Earth and Planetary Interiors, 3, 89–108.

Ross, N.L. (1997) Optical absorption spectra of transition zone minerals and implications for radiative heat transport. Physics and Chemistry of the Earth, 22, 113–118.

Ross, N.L., and Crichton, W.A. (2001) Compression of synthetic hydroxylclinohumite $[Mg_9Si_4O_{16}(OH)_2]$ and hydroxylchondrodite $[Mg_5Si_2O_8(OH)_2]$. American Mineralogist, 86, 990–996.

Sawamoto, H., and Horiuchi, H. (1990) β $(Mg_{0.9}, Fe_{0.1})_2SiO_4$: Single crystal structure, cation distribution, and properties of coordination polyhedra. Physics and Chemistry of Minerals, 17, 293–300.

Sawamoto, H., Weidner, D.J., Sasaki, S., and Kumazawa, M. (1984) Single-crystal elastic properties of the modified spinel (beta) phase of magnesium orthosilicate. Science, 224, 749–751.

Schulze, K., Buchen, J., Marquardt, K., and Marquardt, H. (2017) Multi-sample loading technique for comparative physical property measurements in the diamond-anvil cell. High Pressure Research, 37, 159–169.

Shearer, P.M. (2000) Upper mantle seismic discontinuities. In S. Karato, A. Forte, R. Liebermann, G. Masters, and L. Stixrude, Eds., Earth's Deep Interior: Mineral Physics and Tomography From the Atomic to the Global Scale pp. 115–131. American Geophysical Union, Washington, DC.

Sinogeikin, S.V., Katsura, T., and Bass, J.D. (1998) Sound velocities and elastic properties of Fe-bearing wadsleyite and ringwoodite. Journal of Geophysical Research: Solid Earth, 103, 20819–20825.

Smyth, J.R. (1994) A crystallographic model for hydrous wadsleyite (β-Mg_2SiO_4): An ocean in the Earth's interior? American Mineralogist, 79, 1021–1024.

Smyth, J.R., and Frost, D.J. (2002) The effect of water on the 410-km discontinuity: An experimental study. Geophysical Research Letters, 29, 123.

Smyth, J.R., Kawamoto, T., Jacobsen, S.D., Swope, R.J., Hervig, R.L., and Holloway, J.R. (1997) Crystal structure of monoclinic hydrous wadsleyite [β-$(Mg,Fe)_2SiO_4$]. American Mineralogist, 82, 270–275.

Smyth, J.R., Bolfan-Casanova, N., Avignant, D., El-Ghozzi, M., and Hirner, S.M. (2014) Tetrahedral ferric iron in oxidized hydrous wadsleyite. American Mineralogist, 99, 458–466.

Speziale, S., Duffy, T.S., and Angel, R.J. (2004) Single-crystal elasticity of fayalite to 12 GPa. Journal of Geophysical Research: Solid Earth, 109, B12202.

Stixrude, L., and Lithgow-Bertelloni, C. (2005) Thermodynamics of mantle minerals — I. Physical properties. Geophysical Journal International, 162, 610–632.

——— (2011) Thermodynamics of mantle minerals — II. Phase equilibria. Geophysical Journal International, 184, 1180–1213.

Sumino, Y. (1979) The elastic constants of Mn_2SiO_4, Fe_2SiO_4 and Co_2SiO_4, and the elastic properties of olivine group minerals at high temperature. Journal of Physics of the Earth, 27, 209–238.

Takahashi, T., and Liu, L.-G. (1970) Compression of ferromagnesian garnets and the effect of solid solutions on the bulk modulus. Journal of Geophysical Research, 75, 5757–5766.

Tsuchiya, J., and Tsuchiya, T. (2009) First principles investigation of the structural and elastic properties of hydrous wadsleyite under pressure. Journal of Geophysical Research: Solid Earth, 114, B02206.

Wang, J., Bass, J.D., and Kastura, T. (2014) Elastic properties of iron-bearing wadsleyite to 17.7 GPa: Implications for mantle mineral models. Physics of the Earth and Planetary Interiors, 228, 92–96.

Watt, J.P., Davies, G.F., and O'Connell, R.J. (1976) The elastic properties of composite materials. Reviews of Geophysics, 14, 541–563.

Weidner, D.J., Sawamoto, H., Sasaki, S., and Kumazawa, M. (1984) Single-crystal elastic properties of the spinel phase of Mg_2SiO_4. Journal of Geophysical Research: Solid Earth, 89, 7852–7860.

Wood, B.J. (1995) The effect of H_2O on the 410-kilometer seismic discontinuity. Science, 268, 74–76.

Woodland, A.B., and Angel, R.J. (1998) Crystal structure of a new spinelloid with the wadsleyite structure in the system Fe_2SiO_4-Fe_3O_4 and implications for the Earth's mantle. American Mineralogist, 83, 404–408.

——— (2000) Phase relations in the system fayalite–magnetite at high pressures and temperatures. Contributions to Mineralogy and Petrology, 139, 734–747.

Woodland, A.B., Angel, R.J., and Koch, M. (2012) Structural systematics of spinel and spinelloid phases in the system MFe_2O_4–M_2SiO_4 with M = Fe^{2+} and Mg. European Journal of Mineralogy, 24, 657–668.

Ye, Y., Smyth, J.R., Hushur, A., Manghnani, M.H., Lonappan, D., Dera, P., and Frost, D.J. (2010) Crystal structure of hydrous wadsleyite with 2.8% H_2O and compressibility to 60 GPa. American Mineralogist, 95, 1765–1772.

Yoneda, A., and Morioka, M. (1992) Pressure derivatives of elastic constants of single crystal forsterite. In Y. Syono and M.H. Manghnani, Eds., High-Pressure Research: Application

to Earth and Planetary Sciences pp. 207–214. American Geophysical Union, Washington, DC.

Young, T.E., Green, H.W. II., Hofmeister, A.M., and Walker, D. (1993) Infrared spectroscopic investigation of hydroxyl in β-$(Mg,Fe)_2SiO_4$ and coexisting olivine: Implications for mantle evolution and dynamics. Physics and Chemistry of Minerals, 19, 409–422.

Yusa, H., and Inoue, T. (1997) Compressibility of hydrous wadsleyite (β-phase) in Mg_2SiO_4 by high pressure X-ray diffraction. Geophysical Research Letters, 24, 1831–1834.

Zha, C., Duffy, T.S., Mao, H., Downs, R.T., Hemley, R.J., and Weidner, D.J. (1997) Single-crystal elasticity of β-Mg_2SiO_4 to the pressure of the 410 km seismic discontinuity in the Earth's mantle. Earth and Planetary Science Letters, 147, E9–E15.

Zha, C.-S., Duffy, T.S., Downs, R.T., Mao, H.-K., and Hemley, R.J. (1996) Sound velocity and elasticity of single-crystal forsterite to 16 GPa. Journal of Geophysical Research, 101, 17535–17545.

Zhang, J.S., and Bass, J.D. (2016) Sound velocities of olivine at high pressures and temperatures and the composition of Earth's upper mantle. Geophysical Research Letters, 43, 9611–9618.

Zhao, J., Angel, R.J., and Ross, N.L. (2010) Effects of deviatoric stresses in the diamond-anvil pressure cell on single-crystal samples. Journal of Applied Crystallography, 43, 743–751.

884 **Figure captions**

885 **Figure 1.** Volume and linear compression curves for both crystal sections. Errors are within the
886 size of the symbols. Lines show third-order Birch-Murnaghan EOS curves.

887

888 **Figure 2.** Wadsleyite compositions (end member molar fractions) of the EOS dataset (Tables 5
889 and S4[1]) projected into the ternary diagrams (**a**) Mg_2SiO_4-Fe_2SiO_4-MgH_2SiO_4 and (**b**) Mg_2SiO_4-
890 Fe_2SiO_4-Fe_3O_4. Published EOS and elasticity data cluster around compositions relevant for
891 Earth's mantle with the exception of an isolated data point for $Fe_{2.33}Si_{0.67}O_4$ (Hazen et al. 2000b).
892 The arrows indicate the composition of the present study. H*P*-XRD high-pressure X-ray
893 diffraction, BS Brillouin spectroscopy, UI ultrasonic interferometry, RUS resonant ultrasound
894 spectroscopy, XRD X-ray diffraction (ambient conditions unit cells).

895

896 **Figure 3.** Isothermal bulk moduli for wadsleyite as a function of (**a**) Fe/(Mg+Fe) and (**b**) H_2O
897 molecular equivalents per formula unit. See Table 5 for references. Contours were calculated
898 from the 3-end member model (Table 4). In (**a**), compositions spread vertically for different
899 hydrogen and ferric iron contents. In (**b**), compositions spread vertically for different iron
900 (ferrous and ferric) contents. Solid arrows indicate the composition of the present study. Data
901 points with open symbols were not included in the multi-end member analysis. H*P*-XRD high-
902 pressure X-ray diffraction, BS Brillouin spectroscopy, UI ultrasonic interferometry, RUS
903 resonant ultrasound spectroscopy.

904

905 **Figure 4.** The product of bulk modulus K and mean atomic volume V_A as a function of mean
906 atomic mass M_A for wadsleyites (see Table 5 for references), forsterite (Isaak et al. 1989; Yoneda
907 and Morioka 1992; Zha et al. 1996), fayalite (Sumino 1979; Speziale et al. 2004), Mg-

ringwoodite (Weidner et al. 1984; Jackson et al. 2000; Higo et al. 2006), Fe-ringwoodite (Rigden and Jackson 1991), magnetite (Finger et al. 1986; Reichmann and Jacobsen 2004), hydroxylclinohumite, and hydroxylchondrodite (Ross and Crichton 2001). Bold lines were calculated from the 4-end member model (Table 4). Shaded areas depict uncertainties. Contours in the background show the variation of the bulk sound velocity v_ϕ. H*P*-XRD high-pressure X-ray diffraction, BS Brillouin spectroscopy, UI ultrasonic interferometry, RUS resonant ultrasound spectroscopy.

Footnote

[1] Deposit item AM-00-00000, Supplemental Material including Figures S1 to S8 and Tables S1 to S5.

This is a preprint, the final version is subject to change, of the American Mineralogist (MSA)
Cite as Authors (Year) Title. American Mineralogist, in press.
(DOI will not work until issue is live.) DOI: http://dx.doi.org/10.2138/am-2017-6162

932 **Tables**

933

Table 1. Unit cell parameters and omega scan widths

Crystal	X120	X243
cut || (*hkl*)	(120)	(243)
Unit cell parameters		
a (Å)	5.7062(8)	5.7076(5)
b (Å)	11.4735(10)	11.4736(6)
c (Å)	8.2729(9)	8.2751(6)
V (Å^3)	541.62(11)	541.91(7)
β[a]/°	90.044(9)	90.052(3)
b/*a*	2.0107(3)	2.0102(2)
N[b]	26	26
FWHM[c]		
$\Delta\omega_{MIN}$ (°)	0.060	0.059
$\Delta\omega_{MAX}$ (°)	0.085	0.151
$<\Delta\omega>$ (°)	0.068(6)	0.091(23)

Note: Throughout this paper, standard deviations on the last digit are given in parentheses.

[a] For monoclinic unit cell.

[b] Number of centered reflections.

[c] Full width at half maximum.

934

935

936

937

938

939

Table 2. Unit cell edge lengths and volumes measured at high pressures

Pressure	X120, cut || (120)				X243, cut || (243)			
P (GPa)	*a* (Å)	*b* (Å)	*c* (Å)	*V* (Å^3)	*a* (Å)	*b* (Å)	*c* (Å)	*V* (Å^3)
0.00(3)	5.7087(9)	11.4760(14)	8.2770(7)	542.25(10)	5.7072(5)	11.4770(7)	8.2763(7)	542.11(6)
2.27(4)	5.6858(8)	11.4329(15)	8.2292(7)	534.94(9)	5.6850(7)	11.4297(9)	8.2286(8)	534.68(8)
4.22(4)	5.6691(7)	11.3958(12)	8.1932(6)	529.31(8)	5.6667(6)	11.3961(8)	8.1917(8)	529.01(7)
6.91(4)	5.6448(8)	11.3512(11)	8.1470(6)	522.02(8)	5.6442(5)	11.3501(6)	8.1453(7)	521.81(6)
8.34(4)	5.6335(8)	11.3226(14)	8.1225(6)	518.10(8)	5.6305(4)	11.3257(5)	8.1222(5)	517.95(5)
10.69(4)	5.6128(7)	11.2889(12)	8.0875(6)	512.44(8)	5.6136(6)	11.2884(7)	8.0876(7)	512.50(7)
11.65(6)	5.6065(7)	11.2733(11)	8.0722(6)	510.19(8)	5.6051(5)	11.2723(6)	8.0724(6)	510.04(6)
14.42(6)	5.5837(9)	11.2325(13)	8.0300(6)	503.63(9)	5.5830(6)	11.2286(9)	8.0325(8)	503.56(7)
17.14(8)	5.5643(11)	11.1960(20)	7.9934(9)	497.97(12)	5.5616(8)	11.1910(11)	7.9955(8)	497.64(9)
19.96(12)	5.5450(13)	11.1572(16)	7.9563(8)	492.23(11)	5.5421(8)	11.1500(13)	7.9594(8)	491.85(9)

940

941

942

943

944

945

946

947

948

949

950

951

952

This is a preprint, the final version is subject to change, of the American Mineralogist (MSA)
Cite as Authors (Year) Title. American Mineralogist, in press.
(DOI will not work until issue is live.) DOI: http://dx.doi.org/10.2138/am-2017-6162

953

Table 3. Refined equation of state parameters

Crystal	X120	X243	Combined
3rd order Birch-Murnaghan (BM-3) EOS			
V_0 (Å^3)	542.20(8)	542.05(10)	542.09(7)
K_0 (GPa)	166.7(14)	166.7(20)	166.9(13)
K_0'	4.4(2)	4.4(3)	4.4(2)
a_0 (Å)	5.7086(5)	5.7071(4)	5.7075(3)
b_0 (Å)	11.4765(10)	11.4765(8)	11.4765(7)
c_0 (Å)	8.2762(11)	8.2759(8)	8.2760(7)
k_{10} (GPa)	578(10)	583(8)	583(7)
k_{20} (GPa)	567(10)	580(8)	575(7)
k_{30} (GPa)	398(7)	389(6)	393(5)
k_{10}'	11.4(13)	10.7(12)	10.8(10)
k_{20}'	15.8(15)	12.5(13)	13.9(11)
k_{30}'	12.4(10)	14.5(10)	13.5(8)
2nd order Birch-Murnaghan (BM-2) EOS			
($K_0' = 4$; $k_{10}' = k_{20}' = k_{30}' = 12$)			
V_0 (Å^3)	542.11(8)	542.00(10)	542.03(7)
K_0 (GPa)	169.5(6)	169.1(8)	169.3(5)
a_0 (Å)	5.7087(5)	5.7072(4)	5.7077(3)
b_0 (Å)	11.4750(9)	11.4764(8)	11.4759(6)
c_0 (Å)	8.2759(10)	8.2751(8)	8.2754(7)
k_{10} (GPa)	574(4)	575(3)	576(3)
k_{20} (GPa)	592(4)	583(4)	586(3)
k_{30} (GPa)	401(3)	403(3)	402(2)

954

955

956

957

This is a preprint, the final version is subject to change, of the American Mineralogist (MSA)
Cite as Authors (Year) Title. American Mineralogist, in press.
(DOI will not work until issue is live.) DOI: http://dx.doi.org/10.2138/am-2017-6162

958

Table 4. Calculated second-order Birch-Murnaghan equation of state parameters for wadsleyite end members (Reuss model)

End member	Volume	Isothermal bulk and linear moduli				
	V_0 (Å^3)	K_0 (GPa)	k_{10} (GPa)	k_{20} (GPa)	k_{30} (GPa)	$K_0^{R\,a}$ (GPa)
3-end member model						
Mg_2SiO_4	538.5(2)	169(2)	578(10)	598(9)	404(7)	170(2)
Fe_2SiO_4	569.6(3)	195(22)	718(112)	689(80)	478(79)	203(18)
MgH_2SiO_4	547.5(19)	92(6)	327(35)	242(15)	210(21)	84(4)
4-end member model						
Mg_2SiO_4	538.5(2)	170(2)	580(10)	598(8)	405(7)	170(2)
Fe_2SiO_4	569.6(3)	201(38)	861(246)	780(151)	460(113)	217(32)
MgH_2SiO_4	547.5(19)	92(6)	326(35)	243(15)	209(21)	84(4)
Fe_3O_4	598.5(5)	145(49)	279(65)	405(98)	613(464)	130(27)

[a] $K_0^R = 1/(1/k_{10} + 1/k_{20} + 1/k_{30})$.

959

960

Table 5. Reanalyzed second-order Birch-Murnaghan equation of state parameters for wadsleyites of different compositions

Fe/(Mg+Fe)	H_2O (pfu)	$Fe^{3+}/\sum Fe$	Unit cell edge lengths			Volume	Isothermal bulk modulus		
x	y	z	a_0 (Å)	b_0 (Å)	c_0 (Å)	V_0 (Å^3)	K_0 (GPa)	K_0^R (GPa)	K_0^V (GPa)
0		0	5.73(2)	11.50(5)	8.31(5)	541.5(23)	131.1(155)	95.4(177)	99.4(164)
0		0	5.696(1)	11.453(1)	8.256(1)	538.59(12)		174.3(49)	176.0(33)
0		0	5.6850(7)	11.4406(13)	8.2377(13)	535.75(13)	160.3(26)	159.5(24)	163.9(25)
0		0					168.7(20)		
0	0	0				535.8(2)		168.6(23)	170.1(22)
0		0					164.7(20)		
0		0					170.7(20)		
0		0	5.6972(4)	11.4605(7)	8.2558(7)	539.03(12)	182.4(14)	182.0(8)	187.1(9)
0		0				537.6(1)	171.4(20)		
0		0					168.9(19)		
0.075(10)			5.705(2)	11.450(4)	8.258(3)	539.4(4)		167.4(13)	170.2(13)
0.075(10)			5.705(2)	11.450(4)	8.258(3)	539.4(4)		167.4(13)	170.2(13)
0.08(1)		0.08(2)[d]	5.6984(5)	11.4431(10)	8.2611(11)	538.67(11)	168.8(25)	167.8(22)	174.2(23)
0.08(1)							169.5(12)		
0.091(3)							164.4(1)		
0.091(3)							164.4(1)		
0.12(1)							170.7(20)		
0.13(1)						542.0(3)	170.0(7)		
0.16(1)		0.08(2)[d]	5.7062(5)	11.4566(10)	8.2705(10)	540.65(12)	164.4(24)	164.1(20)	169.4(20)
0.25(1)		0.08(2)[d]	5.7122(7)	11.4887(14)	8.2870(15)	543.81(13)	165.3(27)	164.3(28)	169.2(29)
0.25(1)		0.08(2)[d]	5.7188(5)	11.5093(10)	8.3002(10)	546.30(16)	186.6(20)	186.0(12)	191.7(12)
1		0.28(2)	5.8496(11)	11.8554(19)	8.3774(16)	580.97(30)	176.7(32)	176.5(20)	177.8(21)
0	0.0004(1)	0	5.6982(8)	11.4394(16)	8.2573(16)	538.22(11)	173.0(16)	172.1(22)	177.6(23)
0	0.0288(30)	0	5.6941(2)	11.4597(3)	8.2556(2)	538.70(3)		163.0(15)	165.2(13)
0	0.0295(29)	0	5.7019(9)	11.4650(17)	8.2478(17)	539.15(12)	164.9(12)	164.5(17)	168.7(17)
0	0.0649(61)	0	5.6888(6)	11.4830(8)	8.2523(6)	539.08(8)		159.3(19)	160.7(7)
0	0.0649(58)	0	5.6888(6)	11.4830(8)	8.2523(6)	539.08(8)		158.2(10)	160.0(9)
0	0.0908(83)	0	5.6803(9)	11.5190(19)	8.2496(18)	539.77(9)	159.5(9)	159.0(17)	163.2(17)
0	0.1270(112)	0	5.6722(26)	11.5535(71)	8.2494(58)	540.33(15)	160.8(12)	157.6(46)	163.0(48)
0	0.1270(114)	0	5.6807(3)	11.5243(6)	8.2515(6)	540.20(5)		147.0(9)	148.8(9)
0	0.1894(187)	0	5.6614(13)	11.5526(33)	8.2437(27)	539.01(23)	157.1(23)	155.4(25)	158.8(26)
0	0.1894(187)	0	5.6653(38)	11.5557(86)	8.2473(90)	539.79(88)	145.0(77)	142.8(70)	149.2(72)
0	0.2113(303)	0	5.6766(27)	11.5699(52)	8.2503(49)	541.74(40)	146.7(12)	145.8(14)	148.1(14)
0.10(1)	0.0203(20)	0				541.97(22)	165.7(8)		
0.11(1)	0.1539(153)	0.11(6)	5.6918(10)	11.5276(10)	8.2641(8)	542.23(12)		154.1(12)	155.8(8)
0.11(1)	0.1593(139)	0.11(6)				543.46(19)	153.2(6)		
0.112(2)	0.0192(18)	0.15(3)	5.7077(3)	11.4759(6)	8.2754(7)	542.03(7)	169.3(5)	168.6(5)	173.8(5)

Notes: No entry implies that the respective information was not available. See supplemental online material[1] for further information on data

[a] SX single crystal, PX polycrystal, P powder.

[b] H*P*-XRD high-pressure X-ray diffraction, BS Brillouin spectroscopy, UI ultrasonic interferometry, RUS resonant ultrasound spectroscopy.

[c] MA multi-anvil press, PC piston cylinder press, DAC diamond anvil cell with pressure medium: ME methanol ethanol, MEW methanol

[d] $Fe^{3+}/\sum Fe$ adopted from Fei et al. (1992).

***** Included in multi-end member analysis.

Table 5. (continued)

Isothermal linear moduli			Sample[a]	Method[b]	Environment[c]	Pressure	Reference
k_{10} (GPa)	k_{20} (GPa)	k_{30} (GPa)				P_{MAX} (GPa)	
388(94)	264(66)	243(93)	P	H*P*-XRD	MA	9.6	Mizukami et al. (1975)
576(14)	608(29)	424(12)	SX	BS		0	Sawamoto et al. (1984) *
544(14)	547(14)	384(10)	SX	H*P*-XRD	DAC	4.5	Hazen et al. (1990) *
			PX	UI	MA	12.5	Li et al. (1996)
557(13)	577(12)	416(9)	SX	BS	DAC (Ar/ME/He)	14.2	Zha et al. (1997) *
			PX	UI	PC MA	14.5	Fujisawa (1998)
			PX	UI H*P*-XRD	MA	7.0	Li et al. (1998)
625(5)	621(5)	438(3)	SX	H*P*-XRD	DAC (ME)	10.1	Hazen et al. (2000a) *
			PX	UI H*P*-XRD	MA	7.1	Li et al. (2001)
			PX	RUS		0	Isaak et al. (2007)
563(6)	623(6)	386(4)	SX	BS		0	Sinogeikin et al. (1998) *
563(6)	623(6)	386(4)	SX	BS	DAC (MEW)	17.7	Wang et al. (2014)
575(13)	602(13)	391(9)	SX	H*P*-XRD	DAC	4.5	Hazen et al. (1990) *
			PX	RUS		0	Isaak et al. (2010)
			PX	RUS		0	Katsura et al. (2001)
			PX	RUS		0	Mayama et al. (2004)
			PX	UI	MA	9.6	Li and Liebermann (2000)
			PX	UI H*P*-XRD	MA	12.4	Liu et al. (2009)
592(12)	543(11)	390(8)	SX	H*P*-XRD	DAC	4.5	Hazen et al. (1990) *
548(16)	582(17)	393(11)	SX	H*P*-XRD	DAC	4.5	Hazen et al. (1990) *
634(7)	647(7)	444(5)	SX	H*P*-XRD	DAC (ME)	10.1	Hazen et al. (2000a) *
502(10)	598(12)	500(10)	SX	H*P*-XRD	DAC (ME)	9.0	Hazen et al. (2000b) *
594(13)	595(13)	409(9)	SX	H*P*-XRD	DAC (MEW)	7.3	Holl et al. (2008) *
563(9)	566(9)	386(2)	SX	BS		0	Mao et al. (2008b) *
543(9)	575(10)	400(7)	SX	H*P*-XRD	DAC (MEW)	9.0	Holl et al. (2008) *
535(7)	537(7)	393(9)	SX	BS	DAC (MEW)	12.0	Mao et al. (2008a) *
541(5)	543(5)	380(3)	SX	BS		0	Mao et al. (2008b) *
569(10)	513(9)	387(7)	SX	H*P*-XRD	DAC (MEW)	8.6	Holl et al. (2008) *
615(30)	456(23)	396(20)	SX	H*P*-XRD	DAC (MEW)	9.6	Holl et al. (2008)
516(5)	497(4)	350(2)	SX	BS		0	Mao et al. (2008b) *
568(16)	463(13)	398(11)	P	H*P*-XRD	DAC (MEW)	8.5	Yusa and Inoue (1997) *
534(43)	481(39)	328(28)	SX	H*P*-XRD	DAC (ME)	6.8	Kudoh and Inoue (1998) *
467(8)	496(8)	370(6)	SX	H*P*-XRD	DAC (Ne)	61.3	Ye et al. (2010) *
			SX	H*P*-XRD	DAC (Ne)	31.9	Chang et al. (2015)
559(6)	492(5)	375(4)	SX	BS	DAC (MEW)	12.2	Mao et al. (2011) *
			SX	H*P*-XRD	DAC (Ne)	31.9	Chang et al. (2015)
576(3)	586(3)	402(2)	SX	H*P*-XRD	DAC (Ne)	20.0	This study *

treatment.

ethanol water, Ar argon, He helium, Ne neon.

This is a preprint, the final version is subject to change, of the American Mineralogist (MSA)
Cite as Authors (Year) Title. American Mineralogist, in press.
(DOI will not work until issue is live.) DOI: http://dx.doi.org/10.2138/am-2017-6162

Figure 1

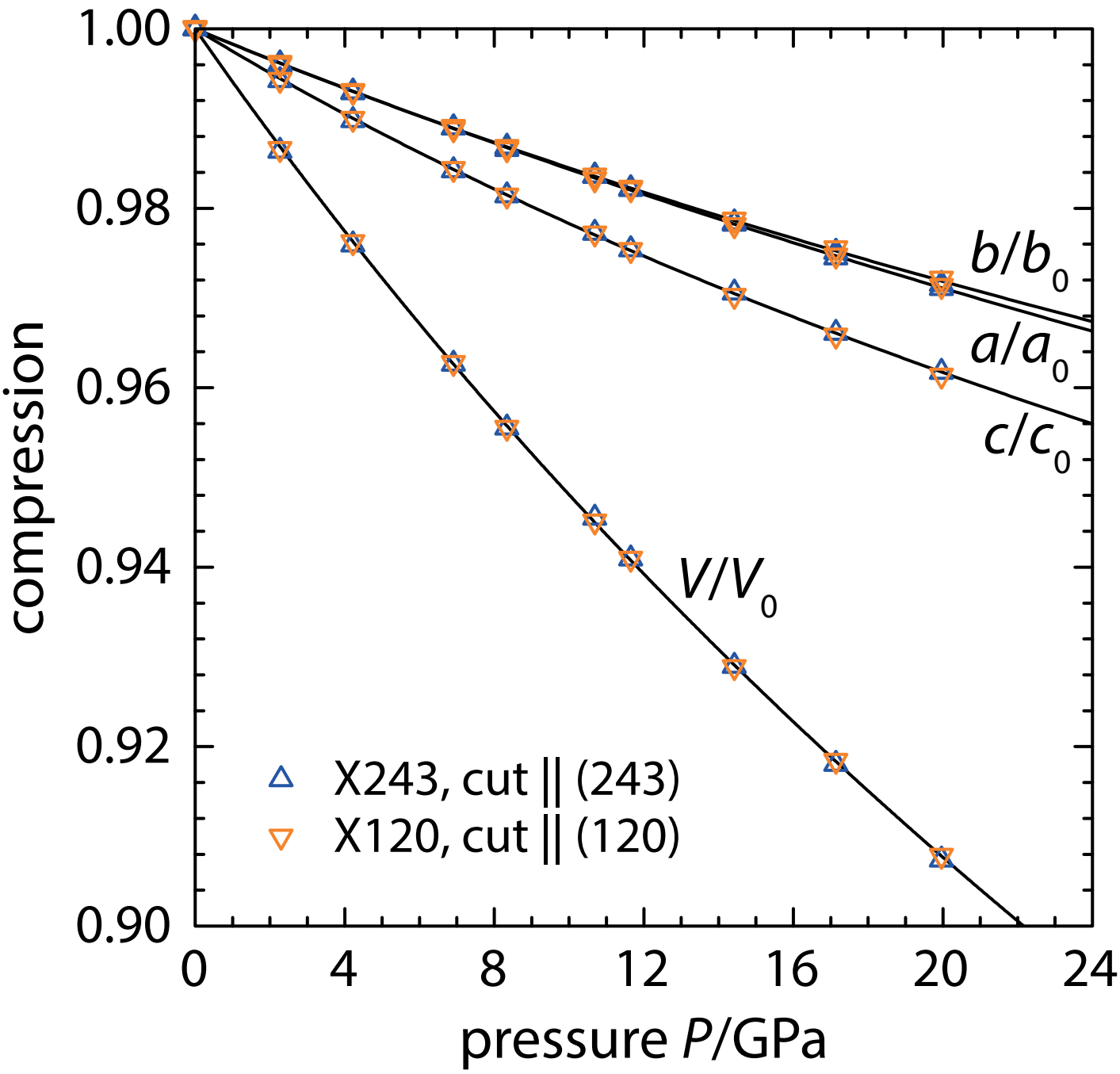

This is a preprint, the final version is subject to change, of the American Mineralogist (MSA)
Cite as Authors (Year) Title. American Mineralogist, in press.
(DOI will not work until issue is live.) DOI: http://dx.doi.org/10.2138/am-2017-6162

Figure 2

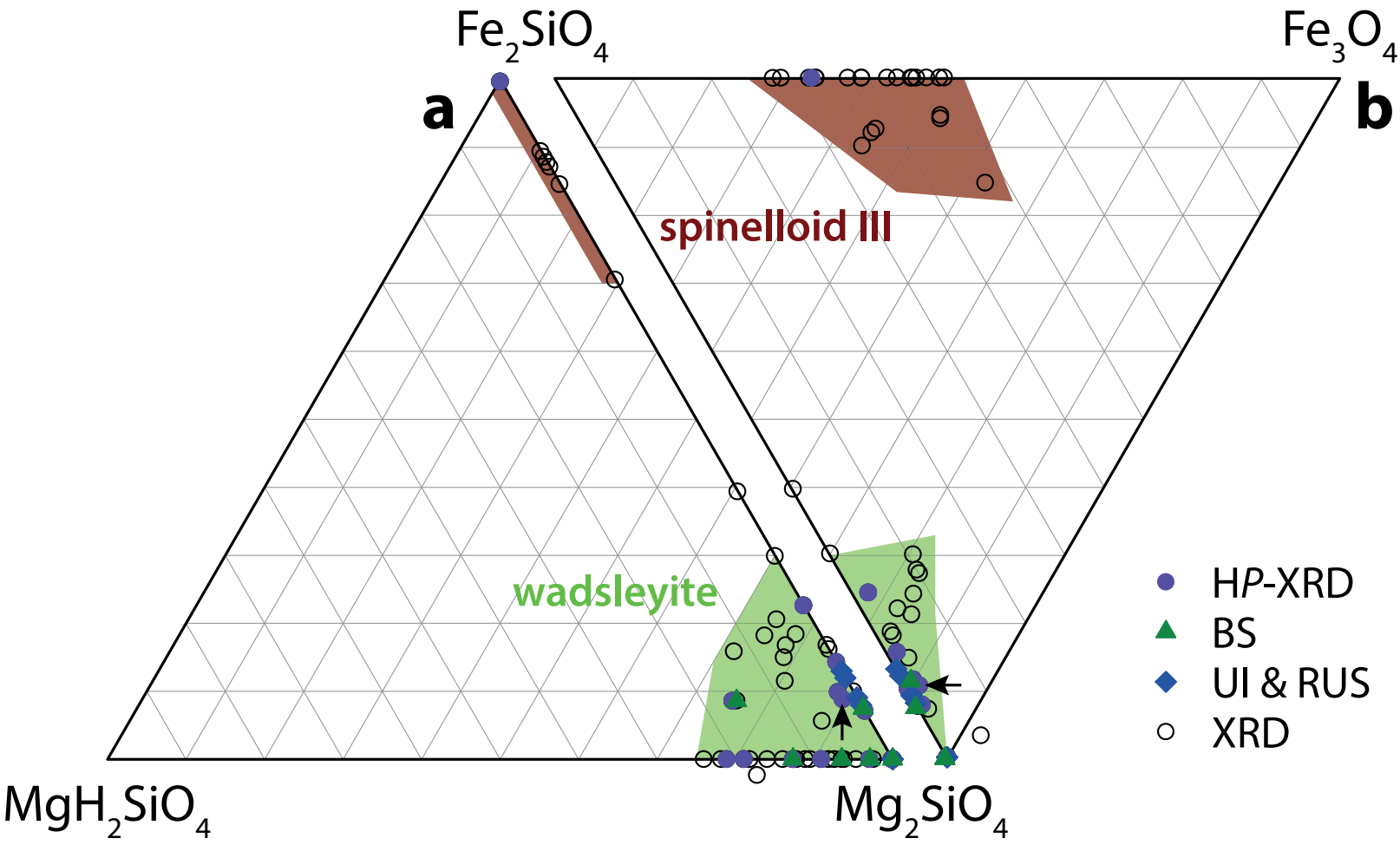

This is a preprint, the final version is subject to change, of the American Mineralogist (MSA)
Cite as Authors (Year) Title. American Mineralogist, in press.
(DOI will not work until issue is live.) DOI: http://dx.doi.org/10.2138/am-2017-6162

Figure 3

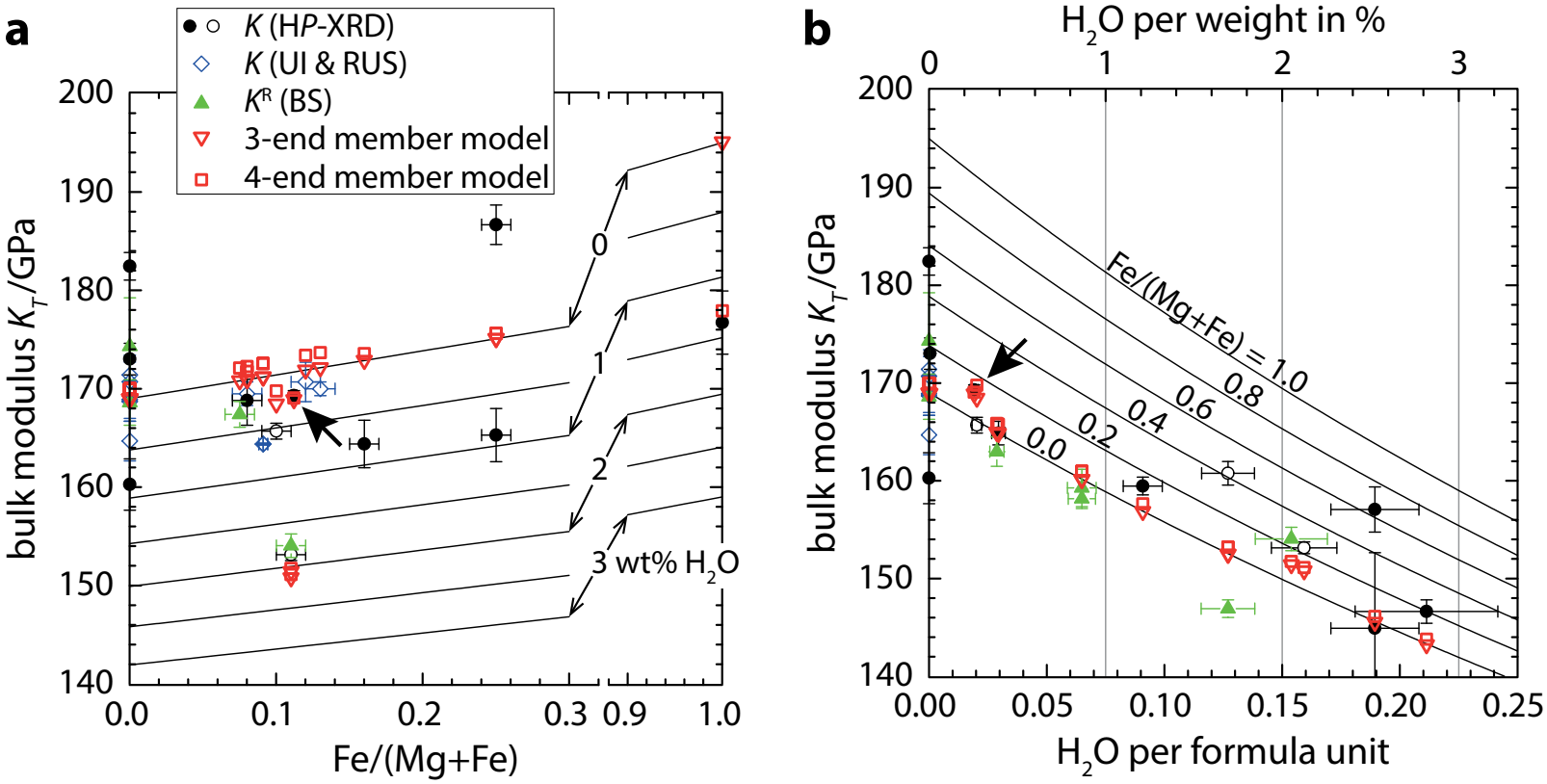

This is a preprint, the final version is subject to change, of the American Mineralogist (MSA)
Cite as Authors (Year) Title. American Mineralogist, in press.
(DOI will not work until issue is live.) DOI: http://dx.doi.org/10.2138/am-2017-6162

Figure 4

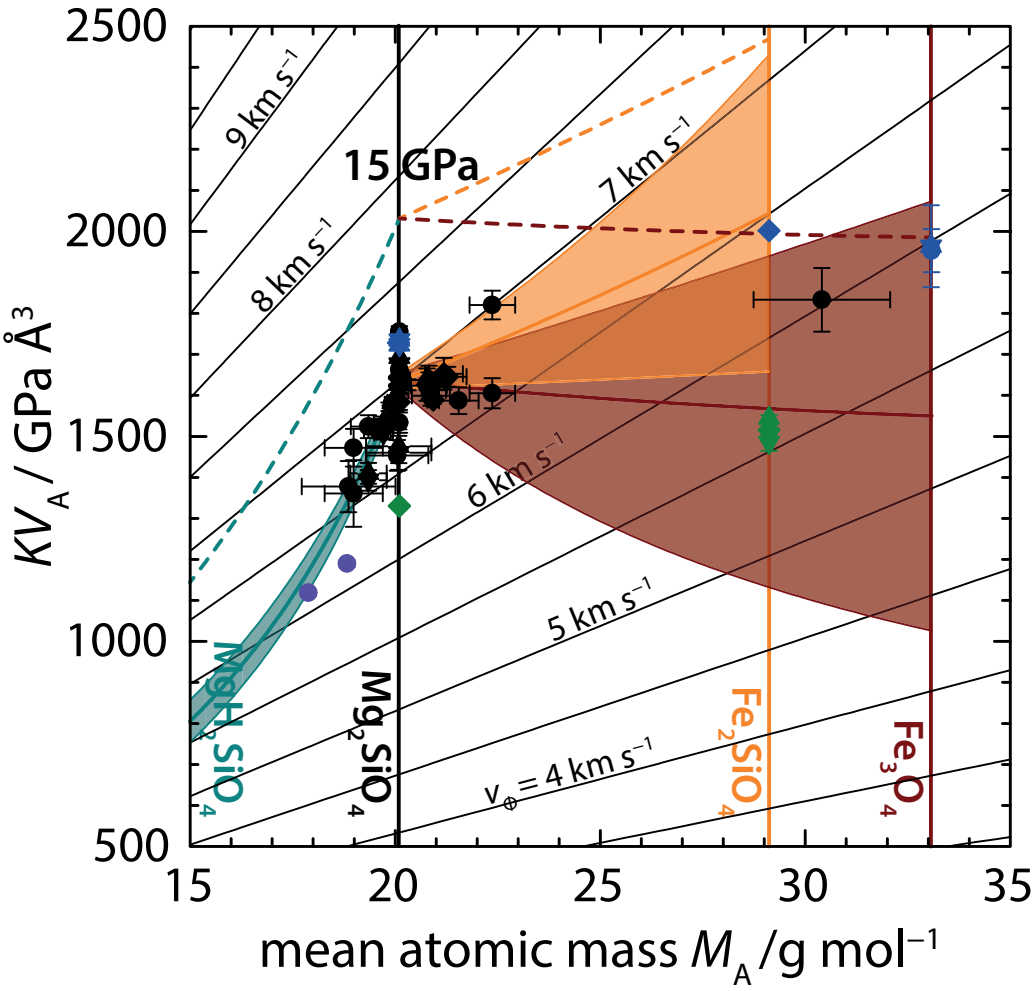

Wadsleyite model
- β-$(Mg,Fe^{2+})_2SiO_4$
- β-$Mg_2SiO_2(O,OH)_2$
- β-$(Mg,Fe^{3+})_2(Si,Fe^{3+})O_4$
- ----- P = 15 GPa

Mineral data
- ●▲▼◆ α (olivine)
- ●▲▼◆ β (wadsleyite)
- ●▲▼◆ γ (ringwoodite)
- ●▲▼◆ n $Mg_2SiO_4 \cdot Mg(OH)_2$
- ○ H*P*-XRD
- △ BS (Voigt)
- ▽ BS (Reuss)
- ◇ UI & RUS